Heliyon 10 (2024) e28359

Contents lists available at ScienceDirect

Heliyon

journal homepage: www.cell.com/heliyon

Research article

Multifaceted chemical and bioactive features of $Ag@TiO_2$ and $Ag@SeO_2$ core/shell nanoparticles biosynthesized using *Beta vulgaris* L. extract

Khaled M. Elattar [a,*], Fatimah O. Al-Otibi [b], Mohammed S. El-Hersh [c], Attia A. Attia [d], Noha M. Eldadamony [e], Ashraf Elsayed [f], Farid Menaa [g], WesamEldin I.A. Saber [c,**]

[a] *Unit of Genetic Engineering and Biotechnology, Faculty of Science, Mansoura University, El-Gomhoria Street, Mansoura, 35516, Egypt*
[b] *Botany and Microbiology Department, Faculty of Science, King Saud University, Riyadh, 11451, Saudi Arabia*
[c] *Microbial Activity Unit, Department of Microbiology, Soils, Water and Environment Research Institute, Agricultural Research Center, Giza, 12619, Egypt*
[d] *Department of Botany and Microbiology, Faculty of Science, Benha University, Benha, Egypt*
[e] *Seed Pathology Department, Plant Pathology Research Institute, Agricultural Research Center, Giza, 12619, Egypt*
[f] *Botany Department, Faculty of Science, Mansoura University, Elgomhouria St., Mansoura, 35516, Egypt*
[g] *Department of Biomedical and Environmental Engineering (BEE), Fluorotronics, Inc. California Innovation Corporation, San Diego, CA 92037, USA*

ARTICLE INFO

Keywords:
Metallic nanoparticles
Characterization
Antifungal
Anti-Hemolysis
Antioxidant
Anti-inflammation

ABSTRACT

Due to increasing concerns about environmental impact and toxicity, developing green and sustainable methods for nanoparticle synthesis is attracting significant interest. This work reports the successful green synthesis of silver (Ag), silver-titanium dioxide ($Ag@TiO_2$), and silver-selenium dioxide ($Ag@SeO_2$) nanoparticles (NPs) using *Beta vulgaris* L. extract. Characterization by XRD, SEM, TEM, and EDX confirmed the successful formation of uniformly distributed spherical NPs with controlled size (25 ± 4.9 nm) and desired elemental composition. All synthesized NPs and the *B. vulgaris* extract exhibited potent free radical scavenging activity, indicating significant antioxidant potential. However, $Ag@SeO_2$ displayed lower hemocompatibility compared to other NPs, while $Ag@SeO_2$ and the extract demonstrated reduced inflammation in a carrageenan-induced paw edema animal model. Interestingly, $Ag@TiO_2$ and $Ag@SeO_2$ exhibited strong antifungal activity against *Rhizoctonia solani* and *Sclerotia sclerotium*, as evidenced by TEM and FTIR analyses. Generally, the findings suggest that *B. vulgaris*-derived NPs possess diverse biological activities with potential applications in various fields such as medicine and agriculture. $Ag@TiO_2$ and $Ag@SeO_2$, in particular, warrant further investigation for their potential as novel bioactive agents.

* Corresponding author.
** Corresponding author.
E-mail addresses: khaledelattar2@yahoo.com (K.M. Elattar), falotibi@ksu.edu.sa (F.O. Al-Otibi), m.elhersh@yahoo.com (M.S. El-Hersh), aaa_attia2005@yahoo.com (A.A. Attia), nohamohamadt@gmail.com (N.M. Eldadamony), ashraf-badawy@mans.edu.eg (A. Elsayed), menaateam@gmail.com (F. Menaa), wesameldin.saber@arc.sci.eg (W.I.A. Saber).

https://doi.org/10.1016/j.heliyon.2024.e28359
Received 15 December 2023; Received in revised form 25 February 2024; Accepted 18 March 2024
Available online 22 March 2024

1. Introduction

The burgeoning field of nanotechnology, manipulating matter at the atomic and nanoscale, offers a revolutionary toolkit for precision medicine and diverse applications [1,2]. In healthcare, the prospect of targeted drug delivery using nanocarriers directly to afflicted cells ignites hope for enhanced efficacy and minimized side effects [3–6]. Nanobiosensors, with their exquisite sensitivity, hold promise for early-stage disease detection at the cellular level, paving the way for timely intervention [7,8]. Furthermore, the field paves the way for tissue regeneration, potentially enabling the repair and restoration of damaged structures [9,10]. However, the impact of nanotechnology transcends healthcare. In the realm of environmental remediation, engineered nanomaterials act as potent catalysts for pollutant degradation, offering solutions for a cleaner future [11–15]. The quest for sustainable energy finds allies in nanotechnology, with innovations such as efficient solar cells and novel energy storage solutions on the horizon [16,17]. Even water purification and disease diagnostics benefit from this technology, with nanofilters and biosensors poised to provide cleaner water and more accurate disease detection methods [18,19]. Moreover, nanotechnology revolutionizes materials science, offering lighter, stronger, and more durable options, while simultaneously contributing to the sustainable production of biofuels [20,21]. Recognizing the potential concerns surrounding the nascent technology, researchers are actively pursuing its responsible development, ensuring the "microscopic revolution" unfolds with safety and ethical considerations at its core [22].

Beta vulgaris L., also known as beetroot, table beet, garden beet, or simply beet, is a widely cultivated biennial plant typically red (although available in yellow, white, or striped forms) belonging to the *Amaranthaceae* family [23]. Beyond its various health benefits [24], *B. vulgaris* offers a wealth of nutrients, including potassium, vitamin C, and folates, alongside non-nutritive components like dietary fibers and polyphenols. Remarkably, beetroot is ranks among the ten most potent vegetables in terms of antioxidant capacity, attributed to its total phenolic content of 50–60 mmol/g dry weight [25]. This impressive antioxidant activity stems from a significant amount of phenolic compounds, including catechin hydrate, protocatechuic acid, epicatechin, ferulic acid, vanillic acid, *p*-hydroxybenzoic acid, *p*-coumaric acid, syringic acid, and caffeic acid [26]. Additionally, beetroot serves as a source of valuable water-soluble nitrogenous pigments called betalains, extensively used in the modern food industry [27,28].

B. vulgaris boasts a high content of antioxidants [29], shielding the body from free radical-induced cellular and molecular damage. This translates to a range of health benefits, including improved blood circulation [30], reduced inflammation [31], a potent cytotoxic effect [32], and a strengthened immune system [33]. Additionally, *B. vulgaris* exhibits diverse biological activities, encompassing hepatoprotective, anti-inflammatory [34], hepatoprotective [35,36], nephroprotective [36,37], cardiovascular protective [36,38], antidiabetic [39], antibacterial [40], and anticancer properties [41,42].

Green synthesis represents a preferred method for fabricating nanoparticles, utilizing natural materials such as plants, microbes, and algae extracts [43–45]. Compared to traditional chemical or physical approaches, this method offers enhanced eco-friendliness, cost-effectiveness, and safety [44,46]. The synthesis process involves reducing metal ions using biological components like polyphenols, which act as both reducing and stabilizing/capping agents, preventing nanoparticle aggregation [47,48]. Current research actively explores developing new and improved green synthesis methods, investigating their potential applications in various fields [49,50].

Mycotoxins, fungal metabolites commonly found on various plant parts, pose significant risks to humans and animals, making them major and unavoidable food contaminants [51]. These toxins, produced by contaminating fungal species like *Sclerotia sclerotium*, *Rhizoctonia solani,* and *Macrophomina phasolina*, cause mycotoxicosis, a chronic disease with potentially detrimental effects [52–55]. Mycotoxins such as aflatoxins, ochratoxins, deoxynivalenol, zearalenone, and fumonisins can have various adverse impacts, including liver toxicity, immune system issues, kidney damage, and birth defects in both animals and humans [51,56]. This urgent threat to food safety necessitates the development of strategies to either inhibit or deactivate fungal contamination in food products.

Hemolysis, the rupture of red blood cells leading to anemia, jaundice, and kidney failure, can be inhibited by various mechanisms. These include membrane stabilization, antioxidant activity, and modulation of specific pro-inflammatory pathways like NF-κB signaling or cytokine production. Anti-inflammatory effects can similarly work through diverse mechanisms, such as suppressing TNF-α and IL-6 signaling, modulating immune cell activity, offering antioxidant protection, and regulating gene expression [57–59]. Understanding these molecular mechanisms holds potential for developing novel therapeutic strategies for various hemolytic and inflammatory diseases, such as sickle cell anemia and arthritis.

The promise of silver nanoparticles (Ag NPs) for antimicrobial applications comes with potential downsides. Researchers raise concerns about their toxicity through oxidative stress, inflammation, genotoxicity, and cytotoxicity [60]. In an attempt to enhance their functionality, combining Ag NPs with other materials like TiO_2 and SeO_2 in core-shell composites seems promising [61]. However, this introduces new safety challenges. These composites can pose additional toxicity risks due to ion release, ROS generation, and size-dependent effects [62–64]. Understanding these multifaceted toxicities is critical to harnessing the benefits of Ag NPs while ensuring their safe and responsible use in various applications.

Following our previous work on green synthesis of metallic NCs using *B. vulgaris* extract [43], this study explores the development and characterization of bimetallic Ag@TiO_2, and Ag@SeO_2 NCs through the same eco-friendly approach. We hypothesize that these bimetallic NCs exhibit enhanced biological activities compared to single-metal Ag NPs. We comprehensively investigate the chemical and biological properties of Ag, Ag@TiO_2, and Ag@SeO_2. Notably, this study pioneers the exploration of the antioxidant, antifungal, anti-hemolytic, and anti-inflammatory activities of these beetroot-derived metallic oxide NCs. These promising results pave the way for developing novel drugs to treat inflammation, fungal infections, and hemolysis.

2. Materials and methods

2.1. Materials

ABTS and DMSO were purchased from Sigma Aldrich (St. Louis, USA). Potassium persulfate was purchased from (Fluka, Biochemical Inc., Bucharest, Romania). Methanol was purchased from El-Nasr Pharmaceutical Chemicals (Cairo, Egypt). Silver nitrate ($AgNO_3$) was purchased from PIOCHEM for laboratory chemicals (CAS Number: 7761-88-8; purity: 99.5%). Selenium dioxide (SeO_2) and titanium dioxide (TiO_2) were purchased from (Merck Schuchardt OHG, 85662, Hohenbrunn, Germany).

2.2. Instruments

Routine state-of-the-art technologies (*i.e.*, UV–Vis spectrophotometry, SEM, TEM, XR, and FTIR) were used. The reads of the absorbance of various tests in this work were accomplished using a Spekol 11 spectrophotometer (analytic Jena AG, Jena, Germany) with a wavelength range of 200–1100 nm. The topography, surface morphology, and elemental compositions of the nanomaterials were examined using SEM and energy dispersive X-ray (EDX) spectroscopy on a Czech FEI SEM-type instrument at an accelerating voltage of 25 kV. TEM analysis was performed on a Thermo Scientific Talos F200i using carbon-coated grids (Type G 200, 3.05 μm diameter, TAAP, USA) was used to analyze the nanomaterials. In addition, TEM-JEM2100-JEOL, Japan was used to analyze the fungus species treated and untreated with Ag@SeO_2 bmNPs. X-ray diffraction (XRD) analysis was performed on a Pan Analytical Philips. Fourier-transform infrared spectroscopy (FTIR) analysis was performed using a Thermo-Fisher Nicolet IS10, USA spectrophotometer.

2.3. Preparation of plant extract and green synthesis of the nanomaterials

Preparation of *B. vulgaris* extract: Fresh *B. vulgaris* plant material was washed, silenced, and dried. An equivalent amount (w/v) of distilled water (ratio 1:10) was added to the dried plant material and soaked at 25 °C overnight. The mixture was then filtered using a Whatman No. 1 filter and used immediately for subsequent experiments.

Synthesis of silver nanoparticles: Separately, silver nanoparticles were synthesized using the *B. vulgaris* extract following a previously reported protocol [43]. Briefly, silver nitrate ($AgNO_3$) and titanium dioxide (TiO_2) or selenium dioxide (SeO_2) were added to the plant extract in a ratio (5:1). The mixture was heated and stirred until a color change was observed (within 5–15 min), indicating nanoparticle formation. The nanomaterials were then purified by centrifugation (10000 rpm, 30 °C), and washed three times with 70% ethanol [65].

2.4. ABTS assay

The established ABTS method [66] was chosen to evaluate the antioxidant potential of the samples. The preparation of the ABTS radical solution involved mixing equal volumes (1:1 v/v) of ABTS solution (7 mM) and potassium persulfate solution (2.45 mM). The mixture was then incubated in the dark at room temperature for 12–16 h. Subsequently, dilution was performed to achieve an absorbance of 0.700 at 734 nm. Individual solutions of the plant extract, Ag NPs, and bimetallic NCs were prepared at varying concentrations. An equal volume of the diluted ABTS solution was then added to each sample tube. These mixtures were kept in the dark at 25 °C for 30 min before measuring their absorbance at 734 nm. Finally, the antioxidant activity was calculated using Equation (1):

$$\text{Radical scavenging activity } (\%) = (\text{Ac} - \text{At}) / \text{Ac} \times 100 \quad (1)$$

Where; 'Ac' is the absorbance of the ABTS radical solution without the antioxidant sample, and 'At' is the absorbance of the mixture of the ABTS radical solution and the antioxidant sample. The IC_{50} values were calculated from a Fit a non-linear regression curve plotted for the percentage of radical scavenging activity versus the sample concentrations. The values of IC_{50} (μg/mL) were expressed as mean ± standard deviation (SD), in which all the tests were run in triplicates.

2.5. Animal model and housing

The study employed male Wistar rats, six weeks old and weighing an average of 169 ± 9.4 g. Prior to experimentation, the rats were provided a one-week acclimation period to their new environment. Throughout the study, they had ad libitum access to rodent chow and tap water. Housing conditions were meticulously controlled, maintaining a temperature of 24 ± 1 °C, humidity of 50 ± 10%, and a 12-h light/12-h dark cycle. All procedures adhered to the guidelines and received approval from the Animal Care and Use Committee (MU-ACUC) of Mansoura University in Egypt.

2.5.1. Anti-hemolytic assay

An anti-hemolytic assay [67] was conducted using blood collected from healthy rats *via* cardiac puncture into heparinized tubes. Plasma was separated from the erythrocytes by centrifugation. The remaining buffy coat was thoroughly washed three times with sterile saline solution (0.89% w/v NaCl, pyrogen-free) using 10 times the volume of the buffy coat in each wash to eliminate any residual plasma. Following each wash, the erythrocytes were centrifuged at 2500 rpm for 10 min to ensure a consistent preparation. The tested materials, *B. vulgaris* extract (57.7 mg/mL), Ag NPs (15.66 mg/mL), Ag@TiO_2 NC (21.62 mg/mL), and Ag@SeO_2 NC (35.16

mg/mL), were individually added to a 10% erythrocytic suspension in phosphate-buffered saline (1X, pH 7.4). All samples were incubated at 37 °C for 45 min. Control groups included: A negative control: containing only saline solution and erythrocyte suspension without any testing material. A positive control: containing distilled water to induce maximum hemolysis. The erythrocyte suspension was centrifuged to separate the intact cells from the lysed cells present in the supernatant. Hemoglobin, the red pigment within erythrocytes, serves as a marker for cell lysis. Therefore, the extent of hemolysis was determined by measuring the absorbance of the supernatant at 540 nm, which corresponds to the absorption wavelength of hemoglobin. To account for background hemolysis, the percentage of hemolysis in the saline control group was subtracted from all other groups. The final percentage of hemolysis for each sample was calculated using Equation (2):

$$\text{Hemolysis } (\%) = \text{Absorbance of sample} \,/\, \text{Absorbance of water control} \times 100 \quad (2)$$

2.5.2. Carrageenan-induced paw edema

The paw edema protocol followed Morris [68]. Carrageenan (1%) was prepared in sterile saline, heated to 90 °C without boiling until fully dissolved, and cooled to room temperature. Selected rats received a subplantar injection of 0.1 mL carrageenan solution into the right hind paw. Tested materials were administered *via* intraperitoneal injection using a vernier caliper. Paw thickness was measured for each rat at baseline (before carrageenan injection) and 0.5, 1, 2, 3, 4, and 5 h after administering the following nanomaterials (57.7 mg/mL B. *vulgaris* extract, 15.66 mg/mL Ag mNPs, 21.62 mg/mL Ag@TiO_2 bmNPs, and 35.16 mg/mL Ag@SeO_2 bmNPs). Additionally, a control group received indomethacin for comparison. The paw was calculated by subtracting the baseline paw thickness from each subsequent measurement. Data were then compared between treated and control groups. The percentage of protection in anti-inflammatory activity can be determined using Equation (3):

$$\text{Protection } (\%) = (1 - (\text{mean of treated group} \,/\, \text{mean of the control group})) \times 100 \quad (3)$$

Control is the average of the anti-inflammatory activity measurements for the group of rats that were not treated with the test compound. Treatment is the average anti-inflammatory activity of the treated group.

2.6. Antifungal activity

Two aggressive plant fungal pathogens, namely *Rhizoctonia solani* (ARC-NW23), and *Sclerotinia sclerotium* (ARC-NW35) were obtained from Seed Pathology Research Department, Plant Pathology Research Institute, Agricultural Research Centre, Giza, Egypt. They were utilized as microbial models for evaluating the potential antifungal activity exerted by the biosynthesized nanomaterials.

MIC Determination of Nanomaterials against Plant Fungal Pathogens: The minimum inhibitory concentration (MIC) of the green Ag NPs, Ag@TiO_2 NC, and Ag@SiO_2 NC (150–1860 μg/mL) against the plant fungal pathogens was evaluated using a broth microdilution assay [69]. Briefly, sterilized flasks containing potato dextrose agar (PDA) medium were prepared, and varying concentrations of each

Fig. 1. Color Transformation in Nanomaterial Synthesis: the transformation of a *Beta vulgaris* L. extract (a) into various nanomaterials: silver nanoparticles (AgNPs, b) and silver-metal oxide nanocomposites (Ag@SeO2 NC, c; Ag@TiO2 NC, d).

nanomaterial were individually incorporated into the molten agar before pouring into Petri dishes. After solidification, a 1 mm diameter disk of each previously grown fungus was individually inoculated onto the center of each plate. Incubation conditions were optimized for each pathogen: *R. solani* (ARC-NW23) incubated at 25 °C for 5 days, while *S. sclerotium* (ARC-NW35) incubated at 18 °C for 7 days. Fungal growth was monitored daily. The MIC was determined as the lowest concentration of nanomaterial that completely inhibited visible fungal growth compared to a control plate containing a PDA medium without any nanomaterial.

2.7. Statistical analysis

Experiments were performed in triplicate for each condition. Data were analyzed using IBM SPSS Statistics version 26 (Armonk, NY, USA). All results are presented as mean ± standard deviation (SD) from at least three independent experiments.

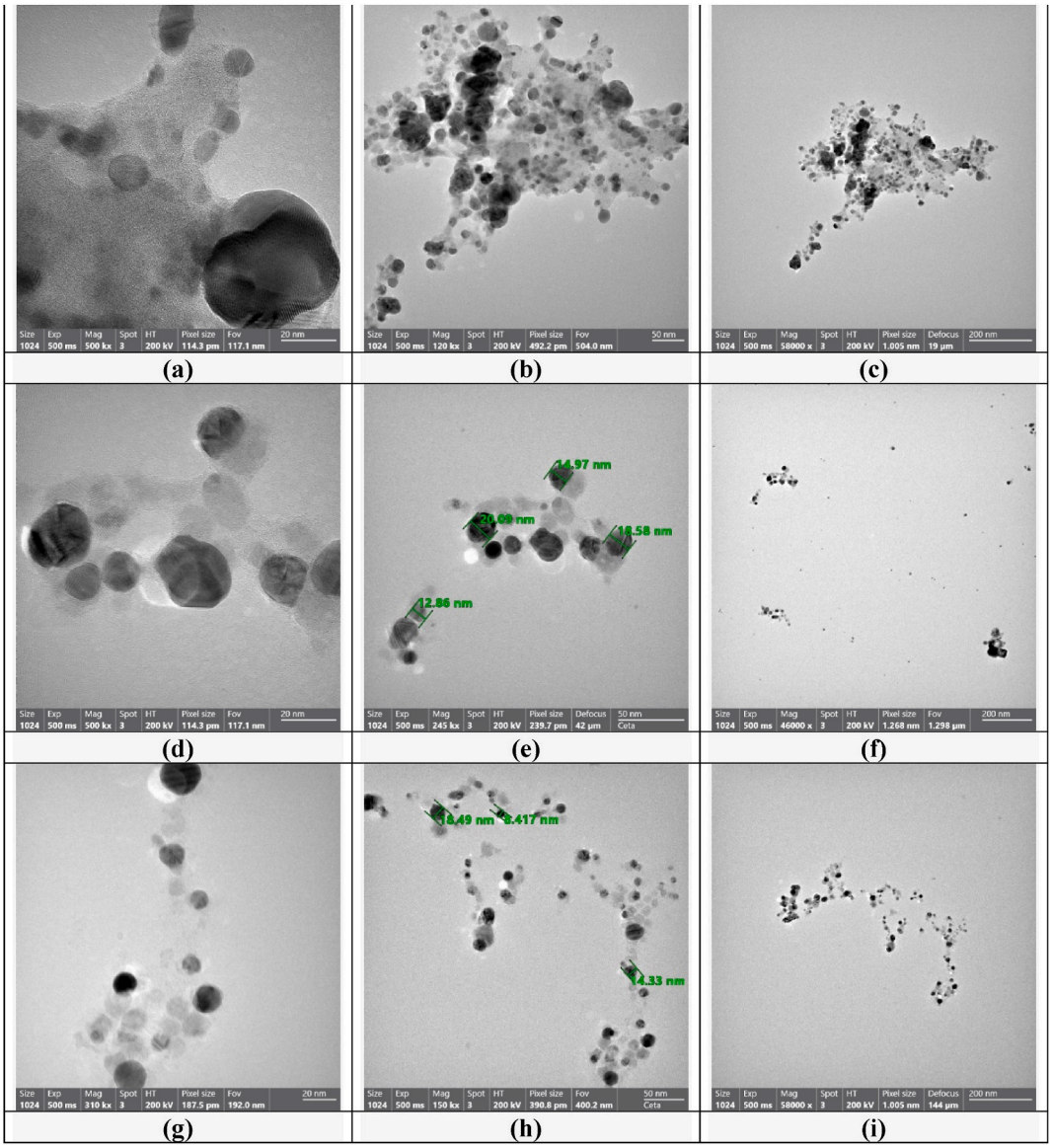

Fig. 2. TEM micrographs of the beet root-mediated nanomaterials' synthesis. **(a–c)** AgNPs; **(d–f)** Ag@TiO_2 NC; **(g–i)** Ag@SeO_2 NC. Nanoparticle sizes range from 5 to 50 nm.

3. Results and discussion

3.1. Physical characterizations of beet roots-mediated metallic nanomaterials

3.1.1. Ultraviolet–visible spectrophotometry (UV–Vis)

B. vulgaris L. aqueous extract successfully mediated the synthesis of silver (Ag), Ag-selenium dioxide (Ag–SeO_2), and Ag-titanium dioxide (Ag@TiO_2) nanoparticles. The initial reddish-brown color of the extract changed to brown for Ag-mNPs, yellow for Ag@SeO_2 bmNPs, and gray for Ag@TiO_2 bmNPs, visually indicating nanoparticle formation (Fig. 1). UV–visible spectroscopy confirmed this, revealing distinct shifts in peak wavelengths due to interactions between metal ions and plant extract components. Ag-mNPs displayed a slightly higher surface plasmon resonance (SPR) peak than expected, suggesting possible aggregation or interaction with plant components. Ag@SeO_2 bmNPs exhibited multiple peaks, while Ag@TiO_2 bmNPs showed a unique peak, indicating differing compositions and interactions. All nanoparticles retained residual absorption peaks at 245–247 nm, likely due to residual plant extract components. The maximum absorption peaks were recorded at λ_{max} ca. 598.0 nm for Ag-mNPs, λ_{max} ca. 428.0 nm for Ag@SeO_2 bmNPs (combined absorption), and λ_{max} ca. 675.0 nm for Ag@TiO_2 bmNPs (combined absorption of Ag and TiO_2) [42]. Different plant extracts have different phytochemical compositions, and the biomolecules in these extracts act as reducing and capping agents during the formation of NPs [44,70].

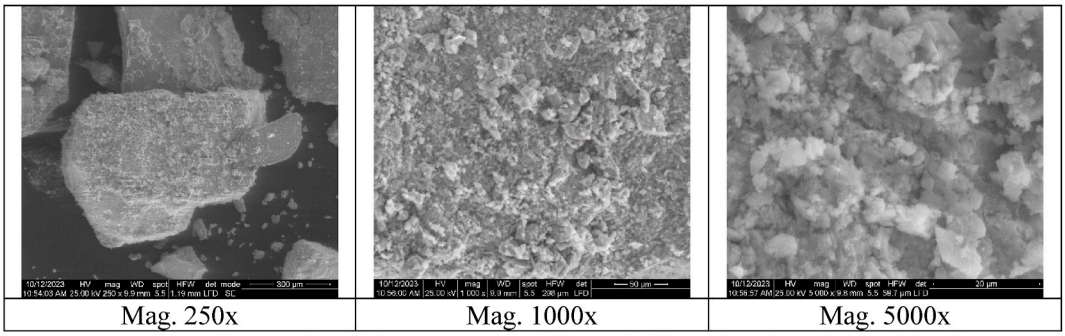

A. SEM micrographs of the Ag NPs at different indicated scales of magnifications.

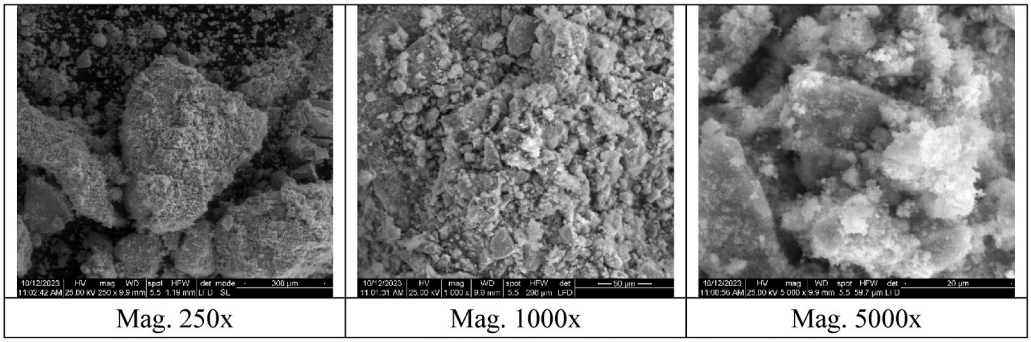

B. SEM micrographs of the Ag@TiO_2 NC at different indicated scales of magnifications.

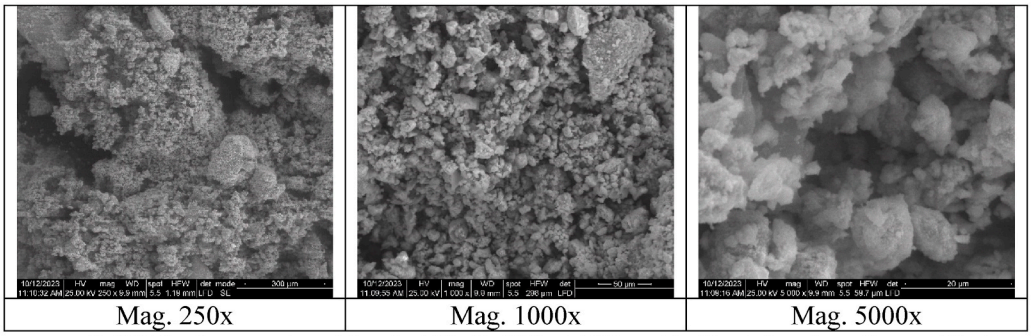

C. SEM micrographs of the Ag@SeO_2 NC at different indicated scales of magnifications.

Fig. 3A. SEM micrographs of the Ag NPs at different indicated scales of magnifications. Fig. 3B. SEM micrographs of the Ag@TiO_2 NC at different indicated scales of magnifications. Fig. 3C. SEM micrographs of the Ag@SeO_2 NC at different indicated scales of magnifications.

3.1.2. Transmission electron microscopy (TEM)

Transmission electron microscopy (TEM) offers valuable insights into the size, size distribution, and shape/morphology of nanoparticles (NPs) [6]. Additionally, TEM can reveal clues about NP interactions, such as aggregation or core-shell structure formation [71]. In this study, TEM analysis of AgNPs, Ag@TiO_2 NC, and Ag@SeO_2 NC prepared from *B. vulgaris* aqueous extract demonstrated well-dispersed and uniform spherical NPs with diameters ranging from 10 to 50 nm (Fig. 2). TEM images of AgNPs specifically revealed typically spherical nanoparticles with sizes between 5 and 20 nm, exhibiting minimal to no aggregation. However, controlling the precise size, size distribution, and shape of these NPs proved challenging (Fig. 2a–c). Notably, aggregation is known to decrease the surface area and catalytic activity of AgNPs [72]. These observations align with previous research demonstrating that lattice fringes arise from the diffraction of the TEM beam by the AgNPs' crystal lattice, with the spacing of these fringes corresponding to the AgNPs' lattice constant [42]. In certain cases, AgNPs may exhibit a distorted crystal structure, potentially due to factors such as the presence of surfactant molecules during synthesis or the NPs' small size [42,72].

The small size and large surface area of silver nanoparticles (AgNPs) contribute to their high surface energy [73]. This, in turn, makes them attractive to each other, leading to aggregation. The surface tension of AgNPs can also contribute to aggregation. Additionally, the inherent surface tension of AgNPs, which is more significant for smaller nanoparticles, further promotes aggregation [73].

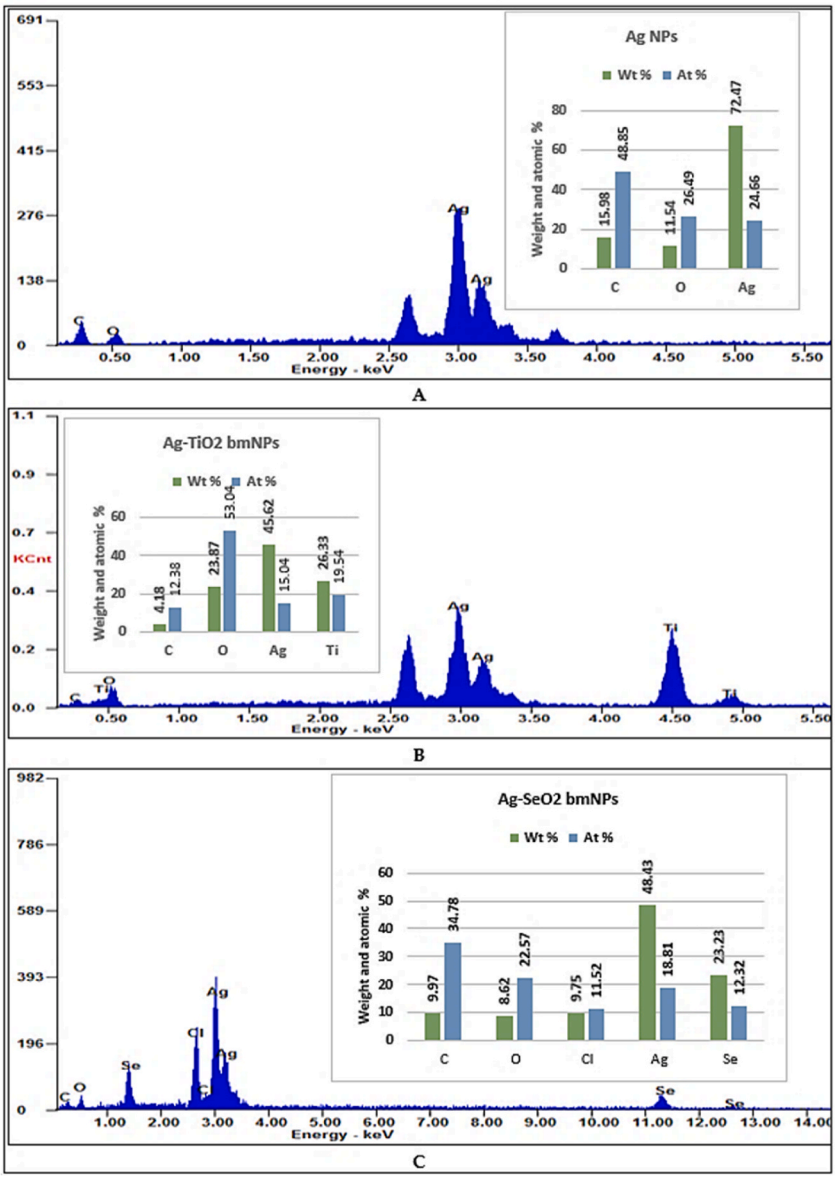

Fig. 4. EDX patterns of **(A)** Ag NPs, **(B)** Ag@TiO_2 NC, and **(C)** Ag@SeO_2 NC.

TEM analysis of the Ag@TiO_2 core/shell magnetic NC revealed sizes ranging from 14.59 to 21.48 nm with a uniform distribution of smaller AgNPs (5–10 nm) decorating the TiO_2 core (Fig. 2d–f). Compared to AgNPs, these Ag@TiO_2 NCs displayed significantly less aggregation. While their larger size might suggest a higher surface energy, their uniform size distribution, and spherical shape mitigate this by minimizing their overall surface energy, leading to greater stability and reduced aggregation tendency. In this composite, the Ag core provides catalytic activity, while the TiO_2 shell shields the silver from oxidation and aggregation [74]. Similarly, TEM images of Ag@SeO_2 core/shell magnetic NC showed spherical NPs with diameters ranging from 10 to 20 nm, again featuring a uniform distribution of smaller AgNPs (5–10 nm) on the SeO_2 core (Fig. 2g–i). The nanoscale of these materials plays a crucial role in their biological and pharmacological activities. Their high surface area-to-volume ratio amplifies their catalytic and optical properties [75].

The antifungal activity of metallic/bimetallic NPs is strongly influenced by their morphology, particularly size and shape [76]. Larger NPs often possess a greater surface area, facilitating interactions with bacterial cell walls and membranes. This enhanced interaction can disrupt cell membranes, leading to leakage of cellular contents and ultimately, cell death [77]. For Ag@SeO_2 NPs, the characteristic "crystal lattice fingerprint" acts as a unique identifier for this specific material. Notably, the low level of aggregation observed in Ag@SeO_2 NPs is advantageous as it prevents the formation of large clumps that could hinder reactivity and reduce surface area [78]. Interestingly, AgNPs appear smaller (5–10 nm) when uniformly distributed on the surface of TiO_2 or SeO_2 NPs compared to their usual size range (5–20 nm). This suggests that at least some AgNPs may be partially embedded within the TiO_2 and SeO_2 matrix. Such interactions with other materials can indeed affect the size, shape, and surface area of NPs, with AgNPs potentially becoming partially encapsulated within the matrix of materials like TiO_2 or SeO_2, leading to a perceived decrease in size [79].

3.1.3. Scanning electron microscopy (SEM)

SEM was implemented to examine the shape/morphology, PS, and PSD of biosynthesized nanomaterials [6]. SEM micrographs were obtained for AgNPs, Ag@TiO_2 NC, and Ag@SeO_2 NC in the reaction medium (Fig. 3A–C). AgNPs (Fig. 3A) appear predominantly spherical, with sizes ranging from 20 to 50 nm. The nanoparticles are densely packed and evenly distributed across the rock surface. Based on the SEM analysis, the estimated particle size of AgNPs falls within a range of 5–10 nm.

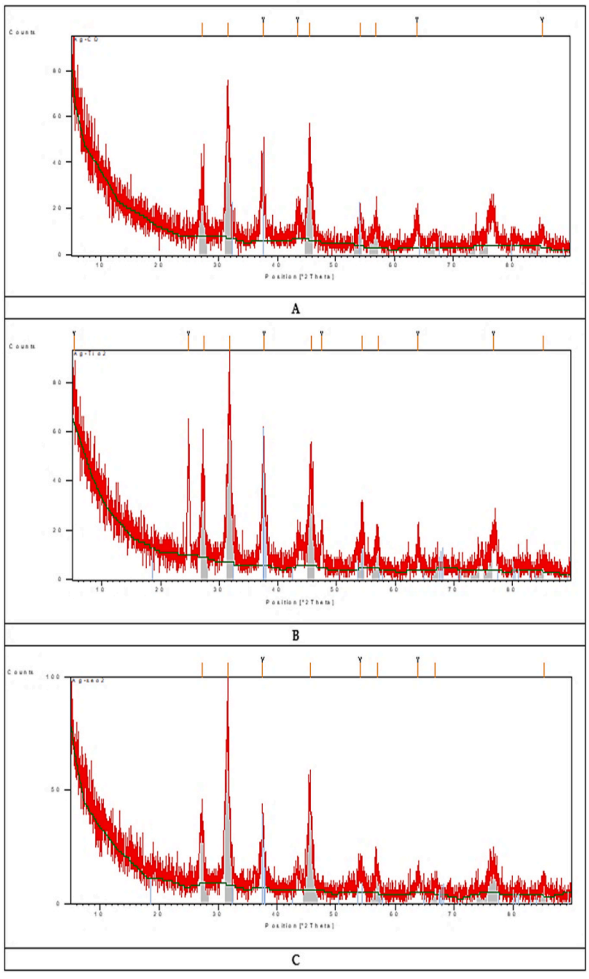

Fig. 5. XRD analysis patterns of **(A)** Ag NPs, **(B)** Ag@TiO_2 NC, and **(C)** Ag@SeO_2 NC.

SEM analysis of Ag@TiO_2 core/shell magnetic NPs (Fig. 3B) reveals spherical particles with a size range of 10–20 nm. Notably, the AgNPs, appearing smaller (5–10 nm), are uniformly distributed and likely partially embedded within the TiO_2 NPs. This observation suggests a porous TiO_2 shell, contributing to the rough surface texture visible in the image [80]. Consistent with expectations, the darker core corresponds to the silver component, while the lighter shell represents the TiO_2 [81]. Similarly, Ag@SeO_2 core/shell magnetic NPs (Fig. 3C) exhibit a spherical morphology with sizes ranging from 10 to 20 nm. As observed for Ag@TiO_2, smaller AgNPs (5–10 nm) are well-dispersed on the SeO_2 NP surface, suggesting potential partial embedding.

3.1.4. Energy-dispersive X-ray spectroscopy (EDX)

Energy-dispersive X-ray spectroscopy (EDX) serves as an indispensable tool in the arsenal of material characterization techniques, offering a non-destructive means to interrogate the elemental composition of diverse materials, including nanoparticles (NPs). Its capabilities extend beyond mere elemental identification, encompassing critical functionalities that drive scientific understanding [6]. The resulting data can be used to understand the structure and properties of the materials and signify potential applications [72].

EDX analysis was performed on AgNPs, Ag@TiO_2 nanocomposites (NCs), and Ag@SeO_2 NCs (Fig. 4A–C, Table S1). Carbon and oxygen were detected in all three samples, likely originating from organic matter like biomolecules [82]. The high silver (Ag) content in all samples confirms it as the primary element (Fig. 4A–C). Examining the relative abundance of elements reveals the highest Ag content in AgNPs, followed by carbon (C) and oxygen (O). This expected outcome confirms the successful green synthesis of AgNPs (Fig. 4A). The presence of titanium (Ti) and selenium (Se) in Ag@TiO_2 NC (Fig. 4B) and Ag@SeO_2 NC (Fig. 4C), respectively, confirms the conjugation of Ag NPs with TiO_2 NPs and SeO_2 NPs to form bimetallic NCs. Notably, Ti and Se rank as the second most abundant elements after Ag in these NCs. In the Ag@SeO_2 NC, the unexpected presence of chlorine (Cl) necessitates further investigation despite its absence in controls. Potential explanations include limitations in EDX sensitivity, masking by other elements, surface binding of chlorides with a stabilizing effect, or contamination within the SeO_2 precursor. Further studies are warranted to definitively determine the source and significance of chlorine in this unique nanomaterial.

3.1.5. X-ray diffraction (XRD) spectroscopy

X-ray diffraction (XRD) analysis offers a robust technique for identifying the crystalline phases present in a sample, determining their relative abundance, and investigating phase transformations in nanoparticles (NPs) [6]. XRD data were acquired for AgNPs, Ag@TiO_2 NC, and Ag@SeO_2 NC (Fig. 5A–C, and Tables S2–S4). The XRD pattern of AgNPs shows several distinct peaks at 2θ values of 27.1430°, 31.4940°, 37.5498°, 43.5437°, 45.5153°, 54.1567°, 56.8317°, 63.8983°, and 85.1594° (Fig. 5A, and Table S2). These characteristic peaks align with the face-centered cubic (fcc) structure of silver, as confirmed by the calculated lattice parameters (Equation (4)):

$$a = 4.0878\ \text{Å} \tag{4}$$

Where, the unit "Å" stands for angstrom, which is a unit of length equal to 10^{-10} m 'a' is the lattice constant of a crystal.

The lattice constant, essentially the length of one side of the repeating unit cell, reflects the fundamental building block size in a crystal structure. In this case, the calculated value of 4.0878 Å defines the unit cell size for the silver crystal structure. This fundamental parameter significantly influences the overall crystal properties. The observed peaks correspond to specific planes within the face-centered cubic (fcc) silver crystal structure: (111), (200), (220), (311), (222), (400), (420), (422), and (511). Notably, the (200) plane exhibits the highest peak intensity, corresponding to 31.4940° 2θ. The calculated lattice parameter of 4.0878 Å closely matches the standard value for fcc silver (4.0862 Å). This excellent agreement reinforces the accuracy of the XRD analysis. Additionally, similar lattice parameters for AgNPs synthesized *via* various methods have been reported in other studies. For example, a coprecipitation method yielded a lattice parameter of 4.0868 Å for AgNPs, and another study reported a range of 4.0860–4.0870 Å for AgNPs synthesized using different techniques [46,83].

The XRD pattern of Ag@TiO_2 NC displays peaks at various 2θ positions (Fig. 5B, and Table S3). The most intense peak at 31.7706° 2θ corresponds to the (101) plane of anatase TiO_2, signifying its presence as the primary phase. However, additional peaks suggest the presence of other phases within the NC. Peaks at 5.3757° and 25.2792° 2θ arise from the (101) and (004) planes of anatase TiO_2, respectively. Additionally, a peak at 47.5269° 2θ corresponds to the (111) plane of metallic silver, confirming its incorporation into the NC. Weaker peaks might be attributed to minor phases like rutile TiO_2 and silver compounds not classified as strictly "metallic" Ag. Overall, the XRD analysis indicates the Ag@TiO_2 NC comprises a combination of anatase and rutile TiO_2 phases alongside metallic silver. Several factors can influence the presence of these phases, including the synthesis method, doping concentration, and annealing temperature. Further analysis can provide more specific information on the relative proportion of each phase and their impact on the overall material properties. The XRD pattern of Ag@SeO_2 NC shows distinct peaks at specific 2θ positions (Fig. 5C, and Table S4). Peaks at 27.3359°, 31.6362°, and 45.6174° 2θ correspond to the (111), (200), and (113) planes of fcc silver, confirming its presence within the NC. However, other peaks suggest the existence of additional phases beyond metallic silver. Peaks at 37.5313°, 54.1235°, and 63.9025° 2θ might indicate the presence of silver compounds, potentially including Ag_2SeO_3. The remaining peaks likely arise from minor phases like SeO_2 and other possible silver compounds, not strictly classified as "metallic" Ag. In summary, the XRD analysis reveals that the Ag@SeO_2 NC comprises a combination of metallic silver and other silver-containing compounds alongside SeO_2. Further analysis could provide more insight into the specific identities and relative proportions of these phases, potentially influencing the overall properties of the nanomaterial.

The XRD patterns of AgNPs, Ag@TiO_2 NC, and Ag@SeO_2 NC all show "metallic" silver phases. However, these patterns reveal further details about their composition: Ag@TiO_2 NC shows peaks corresponding to anatase TiO_2, while the XRD pattern of Ag@SeO_2

NC shows peaks corresponding to other silver compounds, such as $AgSeO_3$ and Ag_2SeO_3. Frequently, the XRD analysis of AgNPs, Ag@TiO_2 NC, and Ag@SeO_2 NC reveals that the NPs are composed of 'metallic' Silver and other phases such as TiO_2 and SeO_2 [84].

Furthermore, XRD analysis can estimate the crystal size of the Ag@TiO_2 NC using the Scherrer Equation (5):

$$D = K\lambda / \beta \cos \theta \quad (5)$$

Where D is the crystal size in nanometers, K is the Scherrer constant (typically 0.9), λ is the wavelength of the X-rays, β is the full width at half maximum intensity (FWHM) (a common measure of the spread of a peak) of the peak in radians, and θ (angular spread or divergence angle) is the Bragg angle in degrees.

The FWHM of the peak at 31.7706 °2Th can be calculated using the following formula (Equation (6)), which describes a relationship between the FWHM of a peak and its θ:

$$FWHM = 2\theta / \text{sqrt}(3) \quad (6)$$

where; sqrt(3), is the square root of 3 (1.732), serving as a scaling factor in the equation and relates to FWHM.

Substituting the measured values of D, K, λ, β, and θ (Bragg angle) into the Scherrer equation (Equation (5)) revealed a crystal size of approximately 20 nm for both Ag@TiO_2 NC and Ag@SeO_2 NC. This finding reinforces the earlier observation that the XRD patterns of these nanomaterials contained peaks corresponding to metallic silver. However, the XRD analysis of Ag@TiO_2 NC yielded further insights beyond metallic silver. Peaks indicative of both anatase and rutile TiO_2 phases were also identified, suggesting the nanoparticles are not solely composed of silver but rather a composite structure combining anatase TiO_2, rutile TiO_2, and metallic silver.

3.2. Antioxidant activity

The ABTS assay relies on the ability of antioxidants to scavenge the ABTS radical. This blue-green radical's characteristic color fades upon interaction with antioxidants, allowing for the measurement of antioxidant activity. Compared to the DPPH method, ABTS offers the advantage of consistent reproducibility across different pH values [66]. The antioxidant activity of beetroot extract, vitamin C (positive control), and biosynthesized nanomaterials was evaluated using varying concentrations ranging from 0 to 100 μg/mL. The

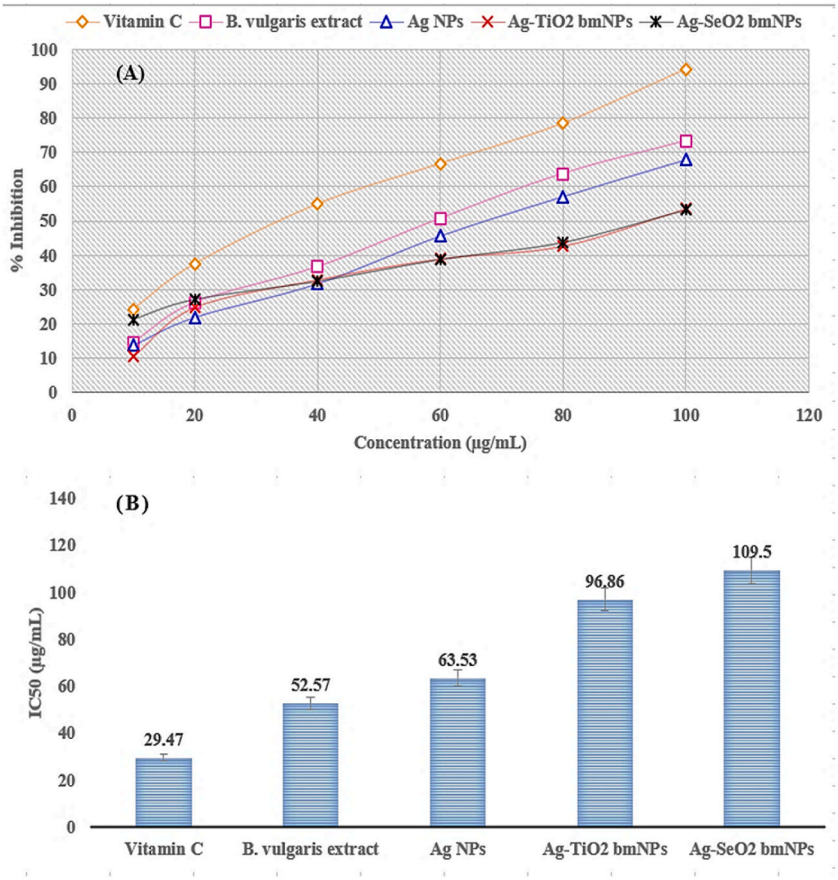

Fig. 6. Concentration-dependent antioxidant activity **(A)**, and IC_{50} **(B)** of the indicated samples by ABTS assay.

results are presented in Fig. 6A and B and Table S5.

Fig. 6A demonstrates a direct correlation between sample concentration and percent scavenging activity. Among the tested samples at 100 μg/mL, vitamin C exhibited the strongest activity (94.3%), followed by the plant extract (73.3%), AgNPs (67.8%), Ag@TiO_2 NC (53.6%), and Ag@SeO_2 NC (53.2%). Between 40 and 100 μg/mL, the plant extract displayed the highest scavenging activity, followed by AgNPs and then both Ag@TiO_2 NC and Ag@SeO_2 NC with similar activity levels. Interestingly, at 40 μg/mL, both Ag@TiO_2 NC and Ag@SeO_2 NC (32.9% and 32.3% respectively) showed higher activity than AgNPs (31.7%). Interestingly, at lower concentrations of 10 and 20 μg/mL, Ag@SeO_2 NC emerged as the most potent scavenger among all samples, with 21.2% and 27% activity, respectively.

All tested samples demonstrated antioxidant activity, but the potency varied across materials. Notably, the *B. vulgaris* extract displayed the strongest activity, with an IC_{50} value of 52.57 μg/mL - approximately half that of ascorbic acid (vitamin C). AgNPs exhibited moderate activity (IC_{50} = 63.53 μg/mL), followed by Ag@TiO_2 NC (IC_{50} = 96.86 μg/mL) and Ag@SeO_2 NC (IC_{50} = 109.5 μg/mL). The potent antioxidant activity of the plant extract likely stems from the presence of phytochemicals like polyphenols and flavonoids, as well as various nutrients like vitamin C, known for scavenging free radicals such as reactive oxygen species (ROS) and reactive nitrogen species [85]. Interestingly, despite potentially utilizing phytochemicals in their synthesis, the overall antioxidant activity of the nanomaterials remained lower than the plant extract. This could be attributed to various factors, including the possible oxidation of phytochemicals during synthesis [86] or the aggregation of nanoparticles, which reduces their surface area and free radical scavenging effectiveness [87].

3.3. Anti-hemolytic activity

Anti-hemolytic activity refers to a material's ability to protect red blood cells (RBCs) from rupturing (lysis). Here, we investigated this activity using hemolysis assays with healthy rat RBCs [6,12]. Hemoglobin (Hb), a red pigment absorbing light at 540 nm, is released from lysed RBCs. Hemolysis activity is assessed by measuring the solution's absorbance at this wavelength. We compared the hemolysis activity of beetroot extract, AgNPs, Ag@TiO_2 NC, and Ag@SeO_2 NC to vitamin C, a known hemocompatible substance (Table 1). Notably, the plant extract and vitamin C showed very similar hemolysis activity, both below 5%. This suggests that the plant extract exhibits anti-hemolytic activity and could be safely administered to humans [6,12]. In contrast, the hemolysis rates of AgNPs (10.97%), Ag@TiO_2 NC (15.77%), and Ag@SeO_2 NC (56.22%) were approximately 2, 3, and 15 times higher than the safety limit. This indicates that these nano-materials are hemotoxic (toxic to blood cells).

Furthermore, the significantly higher hemolysis rates of Ag@TiO_2 NC and Ag@SeO_2 NC compared to AgNPs suggest that bimetallic oxides are more hemotoxic. Notably, a higher hemolysis rate (%) translates to a greater percentage of lysed RBCs [88]. These findings strongly suggest that SeO_2 NPs are not hemocompatible, unlike TiO_2 NPs, based on the differential hemolytic effects observed between each nanomaterial and AgNPs.

Evaluating the hemocompatibility of new drugs, particularly antibiotics, chemotherapeutics, nanodrugs, and oxide nanomaterials, is crucial to differentiate their specific hemolytic effects from other factors contributing to anemia. This differentiation is vital as several conditions and medical interventions can trigger red blood cell (RBC) destruction, including hemolytic anemia, infections, cell anemia, thalassemias, bone marrow aplasia, blood transfusions, and mechanical heart valves [89,90]. Increased hemolysis (measured as % hemolysis) can lead to several complications, such as anemia, organ damage (including kidney and heart failure), jaundice, and gallstones (formed when bilirubin is concentrated in the gallbladder) [89]. The anti-hemolytic assay investigates various mechanisms thought to protect RBCs from damage and lysis. One significant pathway involves antioxidants like vitamin C, which scavenge free radicals and reduce oxidative stress [67].

3.4. Anti-inflammatory activity

The carrageenan-induced paw edema assay, known for its simplicity and reliability, offers a valuable tool for evaluating the anti-inflammatory activity of compounds and drugs [91]. This method leverages the inflammatory response triggered by carrageenan, a seaweed extract, in rat paws, with the expectation that anti-inflammatory agents can mitigate this response [92]. Fig. 7 and Table S6 present the anti-inflammatory activity results, showcasing the protective effect of each sample at various time points. Indomethacin emerged as the most effective agent, providing an average protection of 24.55%. Following closely behind was the *B. vulgaris* extract with a mean protection of 27.86%. Meanwhile, Ag@NPs, Ag@TiO_2, and Ag@SeO_2 demonstrated lower, but still noticeable, anti-inflammatory effects with mean protections of 22.73%, 19.66%, and 5.15%, respectively. In conclusion, this study confirms the

Table 1
Hemolysis activity of the investigated samples.

Investigated compounds	Erythrocyte hemolysis (A/B × 100)	
	Absorbance (A)	Hemolysis, %
The absorbance of pure water (B)	0.875	–
L-ascorbic acid (positive control)	0.030	3.42
***Beta vulgaris* extract**	0.034	3.88
AgNPs	0.096	10.97
Ag@TiO_2 NC	0.138	15.77
Ag@SeO_2 NC	0.492	56.22

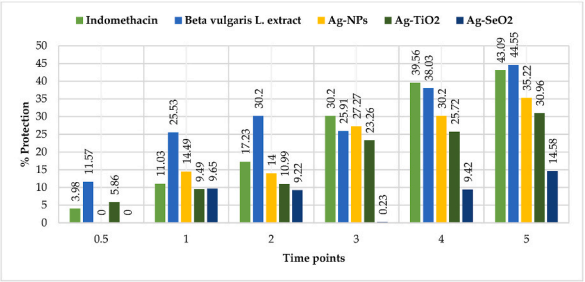

Fig. 7. A comparison of the percentage of protection in the anti-inflammatory activity of the tested samples at varied times.

potent anti-inflammatory properties of both Indomethacin and the *B. vulgaris* extract. While Ag@NPs, Ag@TiO_2, and Ag@SeO_2 also exhibited anti-inflammatory activity, their efficacy was noticeably lower compared to the leading performers.

One possible explanation for the superior anti-inflammatory activity of *B. vulgaris* extract is that it is more effective at inhibiting the production of pro-inflammatory cytokines. Pro-inflammatory cytokines are signaling molecules that play a key role in the inflammatory response. By inhibiting the generation of pro-inflammatory cytokines, *B. vulgaris* extract can reduce inflammation and its associated symptoms. Another possibility is that *B. vulgaris* extract is more effective at promoting the production of anti-inflammatory cytokines. Anti-inflammatory cytokines are signaling molecules that counteract the effects of pro-inflammatory cytokines and help to resolve inflammation. By promoting the production of anti-inflammatory cytokines, *Beta vulgaris* extract can help to speed up the recovery process from inflammation. It is also possible that *Beta vulgaris* L. extract has other mechanisms of action that contribute to its anti-inflammatory activity. For example, it may be able to reduce oxidative stress, which is a major contributor to inflammation, or it may be able to improve the function of the immune system, which can help to fight off infection and reduce inflammation. Generally, the anti-inflammatory data is very promising and recommends that *B. vulgaris* L. extract may be an effective treatment for a variety of inflammatory conditions. Metal nanoparticles have anti-inflammatory activity through a variety of mechanisms [93]. They can inhibit the production of pro-inflammatory cytokines [94,95], promote the production of anti-inflammatory cytokines [96], modulate the function of immune cells, and scavenge reactive oxygen species [97]. The specific mechanism of action varies reliant on the type, size, shape, and surface chemistry of the nanoparticles. In the context of the plant extract, it is possible that the active components are more readily accessible and can interact more effectively with cellular targets compared to the metallic nanoparticles. Additionally, the plant extract may contain a variety of compounds with synergistic effects, contributing to its overall anti-inflammatory activity. However, the results of this study suggest that these agents have the potential to be effective treatments for a variety of inflammatory conditions.

3.5. Antifungal activity

3.5.1. Radial fungal growth

The antifungal activity was evaluated against two targeted pathogenic plant fungi: *Rhizoctonia solani*, and *Sclerotinia sclerotium*. The MIC of each nanomaterial was determined for both fungi (Table 2). Against *R. solani*, the MIC values were 422, 624, and 930 μg/mL for AgNPs, Ag@TiO_2 NC, and Ag@SeO_2 NC, respectively. This indicates that AgNPs and Ag@TiO_2 NC were approximately twice as effective as Ag@SeO_2 NC in inhibiting this fungus. For *S. sclerotium*, the MIC values were 211, 314, and 1390 μg/mL for AgNPs, Ag@TiO_2 NC, and Ag@SeO_2 NC, respectively. Both AgNPs and Ag@TiO_2 NC were roughly 1.5 times more effective than Ag@SeO_2 NC against this fungus. Furthermore, Ag@SeO_2 NC exhibited concentration-dependent antifungal activity. At 422 and 930 μg/mL, it inhibited the growth of *S. sclerotium* by 47.5% and 56.25%, respectively. Notably, even at its MIC threshold of 422 μg/mL, Ag@SeO_2 NC inhibited the growth of *R. solani* by 72.5%. Overall, this study suggests that the antifungal activity of these nanomaterials varies depending on the fungal species and the specific material. While AgNPs and Ag@TiO_2 NC showed broader effectiveness, Ag@SeO_2 NC displayed potent activity against *R. solani* at relatively low concentrations.

Nanoparticles pack a punch against not just bacteria, but also pesky fungi! Studies have shown their effectiveness against both Gram-positive and Gram-negative bacteria, and even specific silver nanoparticles hold promise against fungal foes like *Candida albicans* and *Candida tropicalis* [98,99]. Slavin and Bach [100] reviewed the mechanisms of NPs towards fungal activities across the following modes, *i.e.*, reactive oxygen species, plasma membrane deformation, cell wall architecture, interaction with fungal structure, inhibition of spore germination, and regulation of protein and gene. AgNPs showed potential activity against fungus., *Saccharomyces cerevisiae* KCTC7296, at MIC_{50} (2 μg/mL) [101]. Likewise, the AgNPS, at MIC_{100} (4 μg/mL), was efficient against *Fusarium oxysporum* and at MIC_{100} (1 μg/mL) AgNPs showed potentiality against both *Fusarium solani* and *Aspergillus flavus* [102]. The AgNPs exhibited

Table 2
MIC values (μg/mL) of biosynthesized nanomaterials against some plant pathogenic fungi.

Fungus	Ag NPs	Ag@TiO_2 NC	Ag@SeO_2 NC
Rhizoctonia solani	422	624	930
Sclerotinia sclerotium	211	314	1390

potentiality against *Aspergillus fumigatus* at MIC_{100} (100 μg/mL) [103].

The TiO_2/Ag NPs showed inhibitory activity against *C. albicans* and *Cryptococcus neoformans*, at MIC (12.5 μg/mL) [104]. Selenium NPs showed potential activity against *A. fumigatus* TIMML-050, at MIC value (0.5 μg/mL) [105]. However, The antifungal activity of metallic/bimetallic nanoparticles depends on the nanoparticle's morphology, for instance, size and shape [76]. Larger silver nanoparticles or NC may have a greater surface area, which can promote interactions with bacterial cell walls and membranes, and enhance their antimicrobial activity by causing bacterial cellular contents to leak out [77]. The preparation method produced NPs of various sizes, which caused the antifungal abilities of the nanoparticles to vary visibly. The larger surface area of smaller nanoparticles may explain the significant increase in the capacity of nanopesticides [106]. Nanoparticles with larger surface areas and smaller particle sizes exhibited significantly enhanced antifungal properties thereby inhibiting fungal growth [106].

Our study investigated the antifungal potential of biosynthesized nanomaterials against two major plant pathogens, *Rhizoctonia solani*, and *Sclerotinia sclerotium*. These fungi not only decrease plant growth but also contribute to mycotoxin contamination in food, posing health risks to both animals and humans [52–55]. Interestingly, the nanomaterials exhibited varying antifungal abilities. This variation likely stems from several factors, including the specific type of nanomaterial, its size, and its inherent antimicrobial activity. Previous research suggests that nanoparticles with larger surface areas and smaller sizes tend to demonstrate stronger antifungal properties [106]. Although AgNPs, TiO_2 NPs, and SeO_2 NPs have been shown to exert antifungal activities, the combination of AgNPs with TiO_2 or SeO_2 NPs does not enhance the antifungal activity. There are no additive or synergistic effects. This unexpected failure in enhancing antifungal activity is likely due to factors like competition for fungal binding sites, aggregation, altered surface properties, or interference with AgNP's mechanism of action. Further research is needed to pinpoint the exact reason and optimize nanoparticle design for effective fungal control.

This study demonstrates the strong antioxidant activity of *B. vulgaris* L. extract, suggesting its potential as a natural alternative to harmful fungicides for controlling pathogenic fungi. Its high levels of phenolic and flavonoid constituents are likely contributors to this activity. Furthermore, both plant extracts and nanoparticles can exhibit antifungal activity. One proposed mechanism involves the disruption of membrane-bound respiratory enzymes in fungi, hindering their growth [107]. These findings not only highlight the issue of mycotoxin contamination in food but also offer promising avenues for its control. Ag@SeO2 and Ag@TiO2 NCs, with their antifungal activity, could be explored as safer and potentially more effective alternatives to conventional fungicides in food preservation.

3.5.2. FT-IR spectral analyses on fungi treated with Ag@SeO_2 NC

Ag@SeO_2 NC was chosen for FT-IR analysis since it holds distinct advantages over Ag@TiO_2 NC for FT-IR studies of fungi treated with biosynthesized nanomaterials. Ag@SeO_2 NC holds potential for diverse interaction mechanisms, enhanced specificity for fungal biomolecules, and reduced spectral interference from SeO_2, and the growing interest in their antifungal properties makes them a compelling choice for this research. This selection promises richer data, deeper insights, and broader research impact, solidifying their potential as valuable tools in fungal control. The FT-IR spectral analysis was performed for *R. solani* and *S. sclerotium* treated or not (control) with Ag@SeO_2 NC (Fig. 8). The FTIR spectra obtained for *R. solani*, untreated or treated with Ag@SeO_2 NC, revealed some fascinating variances. The peak in the infrared spectrum at 3279 cm-1 is due to the stretching vibrations of hydroxyl groups. In the treated sample, this peak shifts to a lower frequency (3270 cm-1), suggesting that the Ag@SeO2 NC may be interacting with the –OH

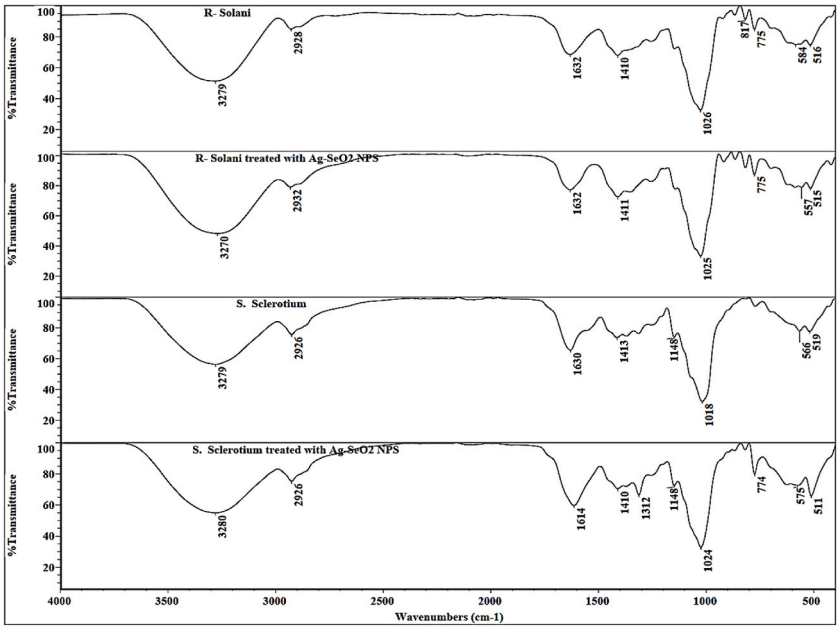

Fig. 8. FTIR spectra of treated or untreated fungi with Ag@SeO_2 NC.

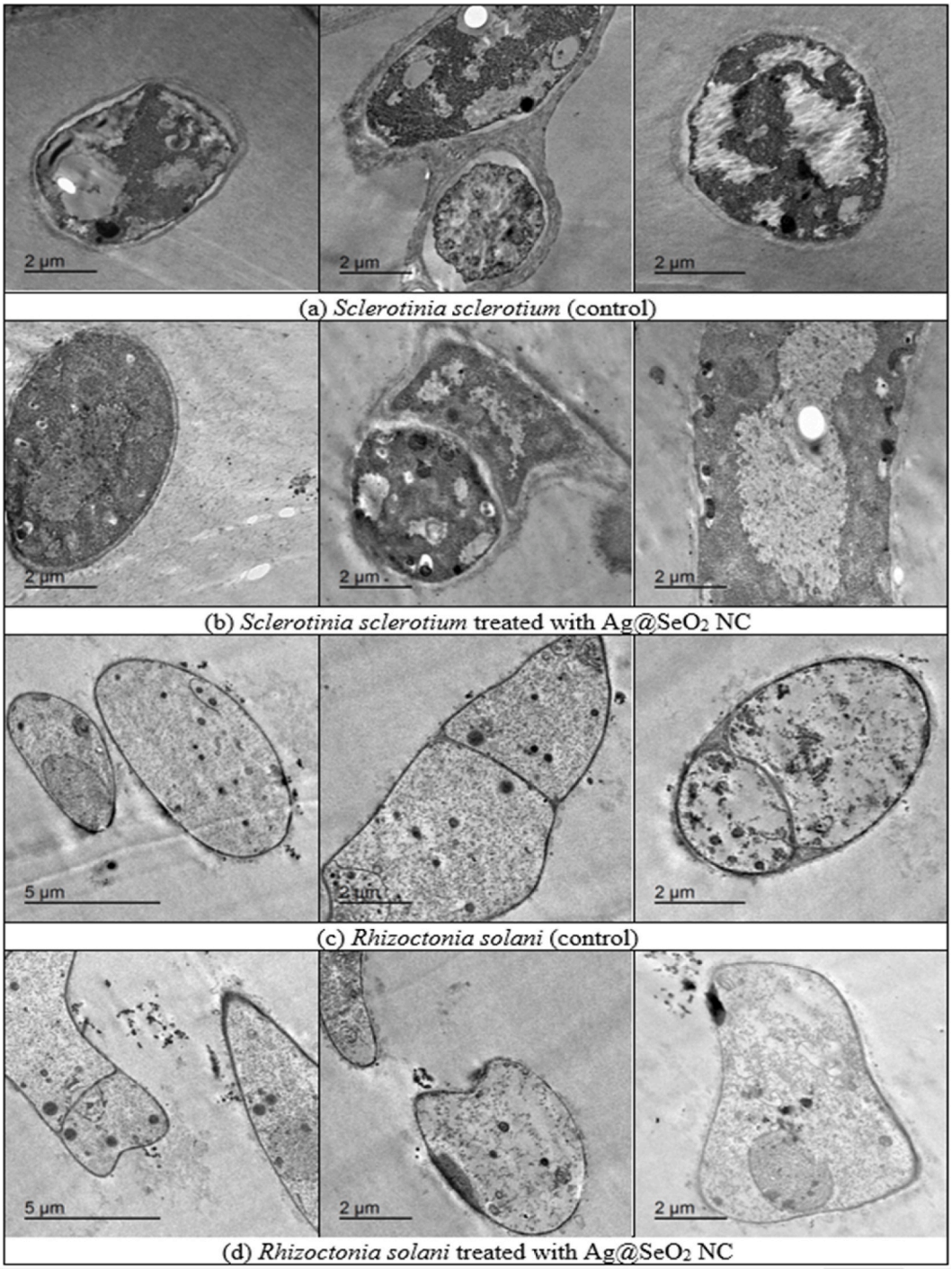

Fig. 9. TEM micrographs reveal the potent antifungal activity of Ag@SeO2 NC against *S. sclerotium* and *R. solani*. Panels (**a**) and (**c**) show the intact cell wall structure of untreated fungal hyphae in both fungi (*S. sclerotium* and *R. solani*, respectively). Treatment with $Ag@SeO_2$ bmNPs in panels (**b**) and (**d**) induces substantial damage to the cell wall and membranes, including disruptions, leakage, and disorganization. These observations demonstrate the ability of $Ag@SeO_2$ NC to effectively penetrate and disrupt the fungal cell structure, leading to potential cell death and fungal growth inhibition. Note the higher magnification used in panels (**c**) and (**d**) to visualize the detailed morphological changes caused by $Ag@SeO_2$ NC treatment.

functions on the surface of the fungal cells [108]. The absorption band at $\nu = 1632\ cm^{-1}$ is attributed to the C═O stretching vibrations of amide functions. The absorption band at $\nu = 817\ cm^{-1}$ is attributed to the C–O stretching vibrations of glycosidic bonds. The disappearance of this band in the treated sample suggests that the Ag@SeO_2 NC may be disrupting the glycosidic bonds in the fungal cell wall [109]. *R. solani* showed a shift in the absorption band at $\nu = 817\ cm^{-1}$ to a lower frequency ($\nu = 775\ cm^{-1}$) after treatment with Ag@SeO_2 NC. This suggests that the nanoparticles may be interacting with the glycosidic bonds in the fungal cell walls.

The FTIR spectra of *S. sclerotium*, untreated or treated with Ag@SeO_2 NC, revealed a shift in the absorption band at $\nu = 3279$ cm-1. The peak in the infrared spectrum at 3279 cm-1 is due to the stretching vibrations of hydroxyl groups. In the treated sample, this peak shifts to a higher frequency (3280 cm-1), suggesting that the Ag@SeO_2 NC may be interacting with the hydroxyl groups on the surface of the fungal cells in a different way than they interact with the surface of *R. solani* cells. The peak in the infrared spectrum at 1630 cm-1 is due to the stretching vibrations of amide groups. The shift of this band to a lower frequency ($\nu = 1614\ cm^{-1}$) in the treated sample suggests that the Ag@SeO_2 NC may be interacting with the amide groups on the surface of the fungal cells in a similar way to how they interact with the amide groups on the surface of *R. solani* cells. The absorption band at $\nu = 1312\ cm^{-1}$ is attributed to the C–N stretching vibrations of chitin. The appearance of this band in the treated sample suggests that the Ag@SeO_2 NC may be interacting with the chitin in the fungal cell wall [110]. The absorption band at $\nu = 566\ cm^{-1}$ is attributed to the C–O stretching vibrations of glycosidic bonds. The disappearance of this band in the treated sample suggests that the Ag@SeO_2 NC may be disrupting the glycosidic bonds in the fungal cell wall, like how they disrupt the glycosidic bonds in the fungal cell wall of *R. solani*. *S. sclerotium* showed a shift in the absorption band at $\nu = 1148\ cm^{-1}$ to a lower frequency ($\nu = 1148\ cm^{-1}$) after treatment with Ag@SeO_2 NC. This suggests that the NCs may be interacting with the C–O bonds in the fungal cell walls [111].

Both *R. solani* and *S. sclerotium* fungal species showed a shift in the absorption band at $\nu = 3279\ cm^{-1}$ to a lower frequency ($\nu = 3270\ cm^{-1}$ and $\nu = 3280\ cm^{-1}$, respectively) after treatment with Ag@SeO_2 NC. This suggests that the NCs may be interacting with the hydroxyl groups (O–H) in the fungal cell walls. Additionally, both species showed a shift in the absorption band at $\nu = 1632\ cm^{-1}$ to a lower frequency ($\nu = 1632\ cm^{-1}$ and $\nu = 1614\ cm^{-1}$, respectively) after treatment with Ag@SeO_2 NC. This suggests that the NCs may also be interacting with the amide groups (C═O–N) in the fungal cell walls.

3.5.3. TEM of the bmNPs-affected fungi

The TEM image of untreated *S. sclerotium* (Fig. 9a) shows a healthy cell with a well-defined cell wall and cytoplasm. The cytoplasm is the jelly-like substance inside the cell that contains all the cell's organelles. The following organelles are visible in the TEM image: mitochondria, ribosomes, nucleus, and vacuole. The TEM image also shows several small vesicles in the cytoplasm. In addition, the cell wall of the *S. sclerotium* cell is a thick, dense layer that surrounds the cell. The cytoplasm also contains a network of microtubules and microfilaments.

The TEM analysis revealed significant damage to *S. sclerotium* cells treated with Ag@SeO_2 NCs (Fig. 9b). Numerous small, dark dots visible within the cell cytoplasm represent the internalized nanoparticles. Moreover, the cell walls exhibited damage, evident from the presence of several holes. Collectively, these observations suggest that Ag@SeO_2 NCs played a role in compromising the cell wall integrity, potentially rendering it more susceptible to further damage [112].

Furthermore, damage extended beyond the cell wall, affecting various organelles within the cytoplasm. Swollen and misshapen mitochondria, for instance, indicate potential interference with the cell's energy production capabilities. In conclusion, the TEM imagery provides compelling evidence for extensive cellular damage inflicted by Ag@SeO_2 NCs on *S. sclerotium*, likely impairing essential functions and compromising overall cell viability (Fig. 9b).

The TEM image of untreated *R. solani* (Fig. 9c) exhibits a healthy cell with a well-defined cell wall and distinct cytoplasmic region. The cytoplasm, a gel-like substance containing various organelles essential for cell function, appears homogeneous in this micrograph. Additionally, small vesicles, membrane-bound structures for transport and storage, are visible within the cytoplasm. The TEM image shows a healthy *R. solani* cell with all of the organelles necessary for the cell to function properly. The cytoplasm of the *R. solani* cell is filled with a variety of organelles, including mitochondria, ribosomes, nuclei, and vacuoles. The cytoplasm also contains a network of microtubules and microfilaments, which provide support and structure for the cell [113]. The *R. solani* cell in the TEM image has a large, well-defined nucleus, which suggests that the cell is healthy and capable of dividing. The *R. solani* cell in the TEM image has a large vacuole, which suggests that the cell is well-hydrated and healthy. Additionally, the *S. sclerotium* cell in the TEM image has several mitochondria, which suggests that the cell is metabolically active [114].

The TEM image of *R. solani* treated with Ag@SeO_2 NCs (Fig. 9d) reveals substantial cellular damage induced by the nanoparticles. Numerous small, dark dots visible within the cytoplasm represent internalized nanoparticles. Moreover, the cell walls exhibit significant damage, evident from the presence of numerous holes. These observations collectively suggest that Ag@SeO_2 NCs contribute to compromised cell wall integrity, potentially rendering it more susceptible to further damage [115]. The damage extends beyond the cell wall, affecting various organelles within the cytoplasm. Notably, some mitochondria appear swollen and misshapen, indicating potential interference with energy production capabilities. Furthermore, the TEM image shows extensive vacuolation within the *R. solani* cell. Vacuolation, characterized by the formation of large vacuoles, represents a type of cell death often observed in response to toxins or stressors [116]. This finding provides additional evidence for the effectiveness of Ag@SeO_2 NCs in killing *R. solani* cells [117].

Generally, there are some hypotheses for possible mechanisms by which the Ag@SeO_2 NC is damaging the *S. sclerotium* and *R. solani* cells: The bmNPs may be generating reactive oxygen species, which are unstable molecules that can damage cell components [42]. The bmNPs may be interacting with the cell membrane, disrupting its structure and function [118]. The bmNPs may be entering the cell and interacting with DNA or other cellular components, causing damage [119].

4. Conclusion

A simple, green, and cost-effective method was established for synthesizing AgNPs, Ag@TiO2 NC, and Ag@SeO2 NC using *B. vulgari* aqueous extract. Comprehensive characterization *via* TEM, SEM, EDX, and XRD confirmed successful nanoparticle formation. Ag@SeO_2 NCs demonstrated potent antifungal activity against *S. sclerotium* and *R. solani* with a minimum inhibitory concentration (MIC) of 462 μg/mL. FT-IR analysis revealed diverse interactions between nanomaterial functional groups and fungal cell walls, suggesting potential mechanisms of action. Although exhibiting the strongest antifungal activity, Ag@SeO_2 NCs also displayed the highest hemolytic activity (56.22%), likely due to the synergistic effect of AgNPs and SeO_2 NPs. Notably, *B. vulgaris* extract itself exerted superior antioxidant activity ($IC_{50} = 52.57$ μg/mL) compared to the synthesized nanomaterials, confirming previous reports. Finally, TEM images corroborated the MIC results, visually confirming the antifungal activity of Ag@SeO_2 NCs against both fungi. These findings showcase the significant chemical features and multifaceted biological activities (antioxidant, anti-hemolytic, and antifungal) of AgNPs, Ag@TiO_2 NCs, and Ag@SeO_2 NCs. While further investigation into specific functionalities and mitigation of Ag@SeO_2 NCs' hemolytic activity is needed, these nanomaterials exhibit promising potential for various industrial and biomedical applications, holding the potential to become candidates for the future development of novel therapeutic agents.

Funding

The authors extend their appreciation to the Researchers Supporting Project number (RSP2024R114), King Saud University, Riyadh, Saudi Arabia.

Institutional review board statement

The ethics consideration of the experimental protocols was approved by the Local Ethics Committee for Animal Experimentation in Animal Care and Use Committee (MU-ACUC), under the approval code; 2024-SREC-005), Mansoura University, 35516, Egypt.

Informed consent statement

Not applicable.

Data availability statement

All data generated or analyzed during this study are included in this published article and the supplementary file.

CRediT authorship contribution statement

Khaled M. Elattar: Writing – original draft, Supervision, Project administration, Formal analysis. **Fatimah O. Al-Otibi:** Funding acquisition. **Mohammed S. El-Hersh:** Methodology, Data curation. **Attia A. Attia:** Writing – review & editing, Investigation. **Noha M. Eldadamony:** Methodology, Data curation, Conceptualization. **Ashraf Elsayed:** Visualization, Validation, Methodology. **Farid Menaa:** Software, Conceptualization. **WesamEldin I.A. Saber:** Writing – review & editing, Writing – original draft, Visualization, Supervision, Methodology, Conceptualization.

Declaration of competing interest

The authors declare that they have no known competing financial interests or personal relationships that could have appeared to influence the work reported in this paper.

Appendix A. Supplementary data

Supplementary data to this article can be found online at https://doi.org/10.1016/j.heliyon.2024.e28359.

References

[1] M. Idrees, Role of nanotechnology in medical sciences: a review, Int. J. Drug Discov. 5 (2015) 14–24.
[2] F. Menaa, When pharma meets nano or the emerging era of nanopharmaceuticals, Pharm. Anal. Acta 4 (2013) 223.
[3] F.A. Khan, R. Albalawi, F.H. Pottoo, Trends in targeted delivery of nanomaterials in colon cancer diagnosis and treatment, Med. Res. Rev. 42 (1) (2022) 227–258.
[4] S. Sahoo, S. Parveen, J. Panda, The present and future of nanotechnology in human health care, in: Nanomedicine in Cancer, 2017, pp. 775–806.
[5] W. Arif, et al., Antibacterial activity of dental composite with ciprofloxacin loaded silver nanoparticles, Molecules 27 (21) (2022) 7182.
[6] H. Iqbal, et al., Breast cancer inhibition by biosynthesized titanium dioxide nanoparticles is comparable to free doxorubicin but appeared safer in BALB/c mice, Materials 14 (12) (2021) 3155.

[7] F. Menaa, A. Abdelghani, B. Menaa, Graphene nanomaterials as biocompatible and conductive scaffolds for stem cells: impact for tissue engineering and regenerative medicine, Journal of tissue engineering and regenerative medicine 9 (12) (2015) 1321–1338.
[8] F. Menaa, Y. Fatemeh, S.K. Vashist, H. Iqbal, O.N. Sharts, B. Menaa, Graphene, an interesting nanocarbon allotrope for biosensing applications: advances, insights, and prospects, in: Biomedical Engineering and Computational Biology, vol. 12, 2021 1179597220983821.
[9] I. Saleem, et al., Effectiveness of Se/ZnO NPs in enhancing the antibacterial activity of resin-based dental composites, Materials 15 (21) (2022) 7827.
[10] U. Wijesinghe, G. Thiripuranathar, F. Menaa, H. Almukhlifi, Eco-friendly synthesis of zinc oxide nanoparticles and assessment of their activities as efficient antioxidant agents, Curr. Nanosci. 19 (1) (2023) 132–146.
[11] N. Zafar, et al., Moringa concanensis-mediated synthesis and characterizations of ciprofloxacin encapsulated into Ag/TiO2/Fe2O3/CS nanocomposite: a therapeutic solution against multidrug resistant E. coli strains of livestock infectious diseases, Pharmaceutics 14 (8) (2022) 1719.
[12] N. Zafar, et al., Green synthesis of ciprofloxacin-loaded cerium oxide/chitosan nanocarrier and its activity against MRSA-induced mastitis, J. Pharmaceut. Sci. 110 (10) (2021) 3471–3483.
[13] Q. Zhang, G. Cao, Nanostructured photoelectrodes for dye-sensitized solar cells, Nano Today 6 (1) (2011) 91–109.
[14] A. Bouafia, et al., Removal of hydrocarbons and heavy metals from petroleum water by modern green nanotechnology methods, Sci. Rep. 13 (1) (2023) 5637.
[15] B. Gherbi, et al., Effect of pH value on the bandgap energy and particles size for biosynthesis of ZnO nanoparticles: efficiency for photocatalytic adsorption of methyl orange, Sustainability 14 (18) (2022) 11300.
[16] S. Haq, et al., A novel shift in the absorbance maxima of methyl orange with calcination temperature of green tin dioxide nanoparticle-induced photocatalytic activity, Catalysts 12 (11) (2022) 1397.
[17] S. Haq, et al., Green synthesis of NiO-SnO2 nanocomposite and effect of calcination temperature on its physicochemical properties: impact on the photocatalytic degradation of methyl orange, Molecules 27 (23) (2022) 8420.
[18] U. Wijesinghe, G. Thiripuranathar, H. Iqbal, F. Menaa, Biomimetic synthesis, characterization, and evaluation of fluorescence resonance energy transfer, photoluminescence, and photocatalytic activity of zinc oxide nanoparticles, Sustainability 13 (4) (2021) 2004.
[19] U. Wijesinghe, G. Thiripuranathar, F. Menaa, H. Iqbal, A. Razzaq, H. Almukhlifi, Green synthesis, structural characterization and photocatalytic applications of ZnO nanoconjugates using Heliotropium indicum, Catalysts 11 (7) (2021) 831.
[20] D. Mamadou, J.S. Duncan, N. Savage, A. Street, R.C. Sustich, Nanotechnology Applications for Clean Water, William Andrew Publishing, 2008.
[21] S.A.H. Martínez, E.M. Melchor-Martínez, J.A.R. Hernández, R. Parra-Saldívar, H.M. Iqbal, Magnetic nanomaterials assisted nanobiocatalysis systems and their applications in biofuels production, Fuel 312 (2022) 122927.
[22] S.F. Ahmed, et al., Utilization of nanomaterials in accelerating the production process of sustainable biofuels, Sustain. Energy Technol. Assessments 55 (2023) 102894.
[23] H. Edziri, et al., Phytochemical analysis, antioxidant, anticoagulant and in vitro toxicity and genotoxicity testing of methanolic and juice extracts of Beta vulgaris L, South Afr. J. Bot. 126 (2019) 170–175.
[24] W.A. Al-Hachami, A.R. Albakaa, N.K. Abed, A.M. Ahmed, N.A. Abdulredha, A.M. Hameed, Comparative evaluation of nutritional values in different food prepared traditional methods from Iraqi cuisine of Beta vulgaris roots, Journal of Hunan University Natural Sciences 49 (1) (2022).
[25] J.A. Vinson, Y. Hao, X. Su, L. Zubik, Phenol antioxidant quantity and quality in foods: vegetables, J. Agric. Food Chem. 46 (9) (1998) 3630–3634.
[26] V.G. Georgiev, J. Weber, E.-M. Kneschke, P.N. Denev, T. Bley, A.I. Pavlov, Antioxidant activity and phenolic content of betalain extracts from intact plants and hairy root cultures of the red beetroot Beta vulgaris cv. Detroit dark red, Plant Foods Hum. Nutr. 65 (2010) 105–111.
[27] J.M. Čanadanović-Brunet, et al., Antioxidant and antimicrobial activities of beet root pomace extracts, Czech J. Food Sci. 29 (6) (2011) 575–585.
[28] S. Kumar, M.S.-L. Brooks, Use of red beet (Beta vulgaris L.) for antimicrobial applications—a critical review, Food Bioprocess Technol. 11 (2018) 17–42.
[29] D. Masih, N. Singh, A. Singh, Red beetroot: a source of natural colourant and antioxidants: a review, J. Pharmacogn. Phytochem. 8 (4) (2019) 162–166.
[30] P. Mirmiran, Z. Houshialsadat, Z. Gaeini, Z. Bahadoran, F. Azizi, Functional properties of beetroot (Beta vulgaris) in management of cardio-metabolic diseases, Nutr. Metabol. 17 (2020) 1–15.
[31] A.A. El Gamal, et al., Beetroot (Beta vulgaris L.) extract ameliorates gentamicin-induced nephrotoxicity associated oxidative stress, inflammation, and apoptosis in rodent model, Mediat. Inflamm. 2014 (2014).
[32] G. J Kapadia, M. A Azuine, G. Subba Rao, T. Arai, A. Iida, H. Tokuda, Cytotoxic effect of the red beetroot (Beta vulgaris L.) extract compared to doxorubicin (Adriamycin) in the human prostate (PC-3) and breast (MCF-7) cancer cell lines, Anti Cancer Agents Med. Chem. 11 (3) (2011) 280–284.
[33] S. Rehman, S. Shah, A.M. Butt, S.M. Shah, Z. Jabeen, A. Nadeem, Biochemical profiling and elucidation of biological activities of Beta vulgaris L. leaves and roots extracts, Saudi J. Biol. Sci. 28 (1) (2021) 592–602.
[34] S. Jain, V.K. Garg, P.K. Sharma, Anti-inflammatory activity of aqueous extract of Beta vulgaris L, J. Basic Clin. Pharm. 2 (2) (2011) 83.
[35] M. Agarwal, V. Srivastava, K. Saxena, A. Kumar, Hepatoprotective activity of Beta vulgaris against CCl4-induced hepatic injury in rats, Fitoterapia 77 (2) (2006) 91–93.
[36] M.J. Ormsbee, J. Lox, P.J. Arciero, Beetroot juice and exercise performance, in: Nutrition and Dietary Supplements, 2013, pp. 27–35.
[37] G. Albasher, et al., Nephroprotective role of Beta vulgaris L. root extract against chlorpyrifos-induced renal injury in rats, Evid. base Compl. Alternative Med. 2019 (2019).
[38] L.G.S. da Silva, et al., Protective effects of beet (Beta vulgaris) leaves extract against oxidative stress in endothelial cells in vitro, Phytother Res. 34 (6) (2020) 1385–1396.
[39] H.S. Mohammed, M.M. Abdel-Aziz, M.S. Abu-Baker, A.M. Saad, M.A. Mohamed, M.A. Ghareeb, Antibacterial and potential antidiabetic activities of flavone C-glycosides isolated from Beta vulgaris subspecies cicla L. var. flavescens (Amaranthaceae) cultivated in Egypt, Curr. Pharmaceut. Biotechnol. 20 (7) (2019) 595–604.
[40] H.S. El-Beltagi, H.I. Mohamed, B.M. Megahed, M. Gamal, G. Safwat, Evaluation of some chemical constituents, antioxidant, antibacterial and anticancer activities of Beta vulgaris L. root, Fresenius Environ. Bull. 27 (9) (2018) 6369–6378.
[41] P. Ninfali, E. Antonini, A. Frati, E.S. Scarpa, C-glycosyl flavonoids from Beta vulgaris cicla and betalains from Beta vulgaris rubra: antioxidant, anticancer and antiinflammatory activities—a review, Phytother Res. 31 (6) (2017) 871–884.
[42] K.M. Elattar, A.A. Ghoniem, F.O. Al-Otibi, M.S. El-Hersh, Y.A. Helmy, W.I. Saber, Phytogenic synthesis and characterization of silver metallic/bimetallic nanoparticles using Beta vulgaris L. Extract and assessments of their potential biological activities, Appl. Sci. 13 (18) (2023) 10110.
[43] P.K. Dikshit, et al., Green synthesis of metallic nanoparticles: applications and limitations, Catalysts 11 (8) (2021) 902.
[44] B. Uzair, et al., Green and cost-effective synthesis of metallic nanoparticles by algae: safe methods for translational medicine, Bioengineering 7 (4) (2020) 129.
[45] O.A. Pivovarov, M.I. Skiba, A.K. Makarova, V.I. Vorobyova, O.O. Pasenko, Preparation of silver nanoparticles by contact nonequilibrium low-temperature plasma in the presence of sodium alginate. Voprosy Khimii i Khimicheskoi Tekhnologii, in: Вопросы хиМии и хиМической технологии, 2017, pp. 82–88, 6.
[46] J. Jeevanandam, Y.S. Chan, M.K. Danquah, Biosynthesis of metal and metal oxide nanoparticles, ChemBioEng Rev. 3 (2) (2016) 55–67.
[47] C.B. Farias, A. Ferreira Silva, R. Diniz Rufino, J. Moura Luna, J.E. Gomes Souza, L.A. Sarubbo, Synthesis of silver nanoparticles using a biosurfactant produced in low-cost medium as stabilizing agent, Electron. J. Biotechnol. 17 (3) (2014) 122–125.
[48] P.G. Jamkhande, N.W. Ghule, A.H. Bamer, M.G. Kalaskar, Metal nanoparticles synthesis: an overview on methods of preparation, advantages and disadvantages, and applications, J. Drug Deliv. Sci. Technol. 53 (2019) 101174.
[49] V. Aswathi, S. Meera, C.A. Maria, M. Nidhin, Green synthesis of nanoparticles from biodegradable waste extracts and their applications: a critical review, Nanotechnology for Environmental Engineering 8 (2) (2023) 377–397.
[50] M. Skiba, A. Pivovarov, V. Vorobyova, T. Derkach, I. Kurmakova, Plasma-chemical formation of silver nanoparticles: the silver ions concentration effect on the particle size and their antimicrobial properties, Journal of Chemical Technology and Metallurgy 54 (2) (2019) 311–318.
[51] S. Amaike, N.P. Keller, Aspergillus flavus, Annu. Rev. Phytopathol. 49 (2011) 107–133.
[52] P. Arora, N. Dilbaghi, A. Chaudhury, Opportunistic invasive fungal pathogen Macrophomina phaseolina prognosis from immunocompromised humans to potential mitogenic RBL with an exceptional and novel antitumor and cytotoxic effect, Eur. J. Clin. Microbiol. Infect. Dis. 31 (2012) 101–107.

[53] L. Azevedo, et al., White mold (Sclerotinia sclerotiorum), friend or foe: cytotoxic and mutagenic activities in vitro and in vivo, Food Res. Int. 80 (2016) 27–35.
[54] R. Cherkupally, S.R. Kota, H. Amballa, B.N. Reddy, In vitro antifungal potential of plant extracts against Fusarium oxysporum, Rhizoctonia solani and Macrophomina phaseolina, Ann. Plant Sci 6 (9) (2017) 1676–1680.
[55] V.H. Khambhati, H.K. Abbas, M. Sulyok, M. Tomaso-Peterson, W.T. Shier, First report of the production of mycotoxins and other secondary metabolites by Macrophomina phaseolina (Tassi) Goid. isolates from soybeans (Glycine max L.) symptomatic with charcoal rot disease, Journal of Fungi 6 (4) (2020) 332.
[56] M.F. Abdallah, G. Girgin, T. Baydar, R. Krska, M. Sulyok, Occurrence of multiple mycotoxins and other fungal metabolites in animal feed and maize samples from Egypt using LC-MS/MS, J. Sci. Food Agric. 97 (13) (2017) 4419–4428.
[57] N. Yahfoufi, N. Alsadi, M. Jambi, C. Matar, The immunomodulatory and anti-inflammatory role of polyphenols, Nutrients 10 (11) (2018) 1618.
[58] M. Tunon, M. Garcia-Mediavilla, S. Sanchez-Campos, J. González-Gallego, Potential of flavonoids as anti-inflammatory agents: modulation of pro-inflammatory gene expression and signal transduction pathways, Curr. Drug Metabol. 10 (3) (2009) 256–271.
[59] N. Boroumand, S. Samarghandian, S.I. Hashemy, Immunomodulatory, anti-inflammatory, and antioxidant effects of curcumin, Journal of Herbmed Pharmacology 7 (4) (2018) 211–219.
[60] Z. Ferdous, A. Nemmar, Health impact of silver nanoparticles: a review of the biodistribution and toxicity following various routes of exposure, Int. J. Mol. Sci. 21 (7) (2020) 2375.
[61] T. Jaswal, J. Gupta, A review on the toxicity of silver nanoparticles on human health, Mater. Today: Proc. 81 (2023) 859–863.
[62] C. Liao, Y. Li, S.C. Tjong, Bactericidal and cytotoxic properties of silver nanoparticles, Int. J. Mol. Sci. 20 (2) (2019) 449.
[63] N. Omerović, et al., Antimicrobial nanoparticles and biodegradable polymer composites for active food packaging applications, Compr. Rev. Food Sci. Food Saf. 20 (3) (2021) 2428–2454.
[64] M.A. Ruiz-Fresneda, S. Schaefer, R. Hubner, K. Fahmy, M.L. Merroun, Exploring antibacterial activity and bacterial-mediated allotropic transition of differentially coated selenium nanoparticles, in: ACS Applied Materials & Interfaces, 2023.
[65] M.M. Hammouda, K. Shalabi, A.A. Alanazi, K.M. Elattar, M.A. Azzam, M.M. Rashed, Synthesis of novel benzopyrimido[4,5-d]azoninone analogs catalyzed by biosynthesized Ag-TiO_2 core/shell magnetic nanocatalyst and assessment of their antioxidant activity, RSC Adv. 13 (46) (2023) 32532–32546.
[66] M. Ozgen, R. Reese, A. Tulio, J. Scheerens, 2, 2-azino-bis-3-ethylbenzothiazoline-6-sulfonic acid (ABTS) method to measure antioxidant capacity of selected small fruits and comparison to ferric reducing antioxidant power (FRAP) and 2, 2′-diphenyl-1-picrylhydrazyl (DPPH), Methods 54 (2006) 1151–1157, https://doi.org/10.1021/jf051960d, 2006.
[67] Z.-G. Yang, H.-X. Sun, W.-H. Fang, Haemolytic activities and adjuvant effect of Astragalus membranaceus saponins (AMS) on the immune responses to ovalbumin in mice, Vaccine 23 (44) (2005) 5196–5203.
[68] C.J. Morris, Carrageenan-induced paw edema in the rat and mouse, in: Inflammation Protocols, 2003, pp. 115–121.
[69] P. Plodpai, S. Chuenchitt, V. Petcharat, S. Chakthong, S.P. Voravuthikunchai, Anti-Rhizoctonia solani activity by Desmos chinensis extracts and its mechanism of action, Crop Protect. 43 (2013) 65–71.
[70] G. Vasyliev, V. Vorobyova, Valorization of food waste to produce eco-friendly means of corrosion protection and "green" synthesis of nanoparticles, Adv. Mater. Sci. Eng. 2020 (2020) 1–14.
[71] G.C. Lavorato, R. Das, J.A. Masa, M.-H. Phan, H. Srikanth, Hybrid magnetic nanoparticles as efficient nanoheaters in biomedical applications, Nanoscale Adv. 3 (4) (2021) 867–888.
[72] N. El-Naggar, W. Saber, A. Zweil, S. Bashir, "An innovative green synthesis approach of chitosan nanoparticles and their inhibitory activity against phytopathogenic Botrytis cinerea on strawberry leaves, Sci. Rep. 12 (2022) 1–20, d, 2022.
[73] S. Shrestha, B. Wang, P. Dutta, Nanoparticle processing: understanding and controlling aggregation, Adv. Colloid Interface Sci. 279 (2020) 102162.
[74] I. Pastoriza-Santos, D.S. Koktysh, A.A. Mamedov, M. Giersig, N.A. Kotov, L.M. Liz-Marzán, One-pot synthesis of Ag@ TiO2 core− shell nanoparticles and their layer-by-layer assembly, Langmuir 16 (6) (2000) 2731–2735.
[75] J.K. Patra, Y. Kwon, K.-H. Baek, Green biosynthesis of gold nanoparticles by onion peel extract: synthesis, characterization and biological activities, Adv. Powder Technol. 27 (5) (2016) 2204–2213.
[76] N. Sher, et al., Comparative study of antimicrobial activity of silver, gold, and silver/gold bimetallic nanoparticles synthesized by green approach, Molecules 27 (22) (2022) 7895.
[77] E. Navarro, et al., Environmental behavior and ecotoxicity of engineered nanoparticles to algae, plants, and fungi, Ecotoxicology 17 (2008) 372–386.
[78] A.-C. Genix, J. Oberdisse, Nanoparticle self-assembly: from interactions in suspension to polymer nanocomposites, Soft Matter 14 (25) (2018) 5161–5179.
[79] J. Jeevanandam, A. Barhoum, Y.S. Chan, A. Dufresne, M.K. Danquah, Review on nanoparticles and nanostructured materials: history, sources, toxicity and regulations, Beilstein J. Nanotechnol. 9 (1) (2018) 1050–1074.
[80] W. Li, et al., A versatile kinetics-controlled coating method to construct uniform porous TiO2 shells for multifunctional core–shell structures, J. Am. Chem. Soc. 134 (29) (2012) 11864–11867.
[81] E. Popovici, et al., Iron/iron oxides core–shell nanoparticles by laser pyrolysis: structural characterization and enhanced particle dispersion, Appl. Surf. Sci. 254 (4) (2007) 1048–1052.
[82] X. Weng, M. Guo, F. Luo, Z. Chen, One-step green synthesis of bimetallic Fe/Ni nanoparticles by eucalyptus leaf extract: biomolecules identification, characterization and catalytic activity, Chem. Eng. J. 308 (2017) 904–911.
[83] Y. Zhang, Z.-R. Tang, X. Fu, Y.-J. Xu, TiO2− graphene nanocomposites for gas-phase photocatalytic degradation of volatile aromatic pollutant: is TiO2− graphene truly different from other TiO2− carbon composite materials? ACS Nano 4 (12) (2010) 7303–7314.
[84] M. Jayapriya, M. Arulmozhi, Beta vulgaris peel extract mediated synthesis of Ag/TiO2 nanocomposite: characterization, evaluation of antibacterial and catalytic degradation of textile dyes-an electron relay effect, Inorg. Chem. Commun. 128 (2021) 108529.
[85] İ. Gülçin, Z. Huyut, M. Elmastaş, H.Y. Aboul-Enein, Radical scavenging and antioxidant activity of tannic acid, Arab. J. Chem. 3 (1) (2010) 43–53.
[86] T. Ahmad, M.A. Bustam, M. Irfan, M. Moniruzzaman, H.M.A. Asghar, S. Bhattacharjee, Mechanistic investigation of phytochemicals involved in green synthesis of gold nanoparticles using aqueous Elaeis guineensis leaves extract: role of phenolic compounds and flavonoids, Biotechnol. Appl. Biochem. 66 (4) (2019) 698–708.
[87] C. Ramamurthy, et al., The extra cellular synthesis of gold and silver nanoparticles and their free radical scavenging and antibacterial properties, Colloids Surf. B Biointerfaces 102 (2013) 808–815.
[88] J. Weisel, R. Litvinov, Red blood cells: the forgotten player in hemostasis and thrombosis, J. Thromb. Haemostasis 17 (2) (2019) 271–282.
[89] B. Fattizzo, W. Barcellini, Autoimmune hemolytic anemia: causes and consequences, Expet Rev. Clin. Immunol. 18 (7) (2022) 731–745.
[90] F. Menaa, Stroke in sickle cell anemia patients: a need for multidisciplinary approaches, Atherosclerosis 229 (2) (2013) 496–503.
[91] O.O. Adegbenro, O.T. Opeyemi, Development and estimation of anti-inflammatory activity of topical etoricoxib emulgel by carrageenan induced paw oedema method, Univers. J. Pharm. Res 4 (2019) 23–28.
[92] Z. Ou, et al., Anti-inflammatory effect and potential mechanism of betulinic acid on λ-carrageenan-induced paw edema in mice, Biomed. Pharmacother. 118 (2019) 109347.
[93] A. Gomes, E. Fernandes, J.L. Lima, L. Mira, M.L. Corvo, Molecular mechanisms of anti-inflammatory activity mediated by flavonoids, Curr. Med. Chem. 15 (16) (2008) 1586–1605.
[94] J.-M. Cavaillon, Pro-versus anti-inflammatory cytokines: myth or reality, Cellular And Molecular Biology-Paris-Wegmann- 47 (4) (2001) 695–702.
[95] V.V. Sumbayev, et al., Gold nanoparticles downregulate interleukin-1β-induced pro-inflammatory responses, Small 9 (3) (2013) 472–477.
[96] K.K. Wong, et al., Further evidence of the anti-inflammatory effects of silver nanoparticles, ChemMedChem: Chemistry enabling drug discovery 4 (7) (2009) 1129–1135.
[97] T. Yoshitomi, Y. Nagasaki, Reactive oxygen species-scavenging nanomedicines for the treatment of oxidative stress injuries, Adv. Healthcare Mater. 3 (8) (2014) 1149–1161.

[98] K. Chand, et al., Photocatalytic and antimicrobial activity of biosynthesized silver and titanium dioxide nanoparticles: a comparative study, J. Mol. Liq. 316 (2020) 113821.
[99] E.J.J. Mallmann, F.A. Cunha, B.N. Castro, A.M. Maciel, E.A. Menezes, P.B.A. Fechine, Antifungal activity of silver nanoparticles obtained by green synthesis, Revista do instituto de Medicina Tropical de sao Paulo 57 (2015) 165–167.
[100] Y.N. Slavin, H. Bach, Mechanisms of antifungal properties of metal nanoparticles, Nanomaterials 12 (24) (2022) 4470.
[101] K.-J. Kim, et al., Antifungal activity and mode of action of silver nano-particles on Candida albicans, Biometals 22 (2009) 235–242.
[102] D. Wang, B. Xue, L. Wang, Y. Zhang, L. Liu, Y. Zhou, Fungus-mediated green synthesis of nano-silver using Aspergillus sydowii and its antifungal/antiproliferative activities, Sci. Rep. 11 (1) (2021) 10356.
[103] A. Auyeung, et al., Effective control of molds using a combination of nanoparticles, PLoS One 12 (1) (2017) e0169940.
[104] F. Martinez-Gutierrez, et al., Synthesis, characterization, and evaluation of antimicrobial and cytotoxic effect of silver and titanium nanoparticles, Nanomed. Nanotechnol. Biol. Med. 6 (5) (2010) 681–688.
[105] M.H. Bafghi, R. Nazari, M. Darroudi, M. Zargar, H. Zarrinfar, The effect of biosynthesized selenium nanoparticles on the expression of CYP51A and HSP90 antifungal resistance genes in Aspergillus fumigatus and Aspergillus flavus, Biotechnol. Prog. 38 (1) (2022) e3206.
[106] E. El-Argawy, M. Rahhal, A. El-Korany, E. Elshabrawy, R. Eltahan, Efficacy of some nanoparticles to control damping-off and root rot of sugar beet in El-Behiera Governorate, in: J. Asian (Ed.), Plant Pathol. 11 (1) (2017) 35–47.
[107] J. Narware, R. Yadav, C. Keswani, S. Singh, H. Singh, Silver nanoparticle-based biopesticides for phytopathogens: scope and potential in agriculture, in: Nano-biopesticides Today and Future Perspectives, Elsevier, 2019, pp. 303–314.
[108] E. Priyadarshini, S.S. Priyadarshini, B.G. Cousins, N. Pradhan, Metal-Fungus interaction: review on cellular processes underlying heavy metal detoxification and synthesis of metal nanoparticles, Chemosphere 274 (2021) 129976.
[109] R. Ghamari, A. Ahmadikhah, M. Tohidfar, M.R. Bakhtiarizadeh, RNA-seq analysis of magnaporthe grisea transcriptome reveals the high potential of ZnO nanoparticles as a nanofungicide, Front. Plant Sci. 13 (2022) 896283.
[110] A.M.R. Gherman, N.E. Dina, V. Chiş, A. Wieser, C. Haisch, Yeast cell wall–Silver nanoparticles interaction: a synergistic approach between surface-enhanced Raman scattering and computational spectroscopy tools, Spectrochim. Acta Mol. Biomol. Spectrosc. 222 (2019) 117223.
[111] K. Mukherjee, K. Acharya, A. Biswas, N.R. Jana, TiO2 nanoparticles co-doped with nitrogen and fluorine as visible-light-activated antifungal agents, ACS Appl. Nano Mater. 3 (2) (2020) 2016–2025.
[112] Y. Jabalera, M. Montalban-Lopez, J. Vinuesa-Rodriguez, G. Iglesias, M. Maqueda, C. Jimenez-Lopez, Antibacterial directed chemotherapy using AS-48 peptide immobilized on biomimetic magnetic nanoparticles combined with magnetic hyperthermia, Int. J. Biol. Macromol. 189 (2021) 206–213.
[113] A. Kowaltowski, F. Abdulkader, A. Kowaltowski, F. Abdulkader, Mitochondria: the batteries of our cells, in: Where Does All that Food Go? How Metabolism Fuels Life, 2020, pp. 37–49.
[114] H. Liao, et al., Integrated proteomic and metabolomic analyses reveal significant changes in chloroplasts and mitochondria of pepper (Capsicum annuum L.) during Sclerotium rolfsii infection, J. Microbiol. 60 (5) (2022) 511–525.
[115] M.M. Eltarahony, A. Kamal, Biogenic metals/metal oxides nanocomposites as eco-friendly antagonistic agents, in: Biogenic Nanomaterial for Health and Environment, CRC Press, 2024, pp. 125–139.
[116] A.V. Shubin, I.V. Demidyuk, A.A. Komissarov, L.M. Rafieva, S.V. Kostrov, Cytoplasmic vacuolization in cell death and survival, Oncotarget 7 (34) (2016) 55863.
[117] A.M. Ismail, Efficacy of copper oxide and magnesium oxide nanoparticles on controlling black scurf disease on potato, Egypt. J. Phytopathol. 49 (2) (2021) 116–130.
[118] A.G. Rodríguez-Hernández, R. Vazquez-Duhalt, A. Huerta-Saquero, Nanoparticle-plasma membrane interactions: thermodynamics, toxicity and cellular response, Curr. Med. Chem. 27 (20) (2020) 3330–3345.
[119] C. Buzea, I.I. Pacheco, K. Robbie, Nanomaterials and nanoparticles: sources and toxicity, Biointerphases 2 (4) (2007) MR17–MR71.